

# JGR Solid Earth

## RESEARCH ARTICLE

10.1029/2022JB025749

### Key Points:

- A phase-field investigation illuminating the etch-pitting behavior on the surface of K-feldspar and its impact on reservoir quality
- A novel simulation-based workflow for capturing the etch-pitting phenomena in sandstone up to three orders of magnitude larger
- Orientation of etch-pits and volume percentage of K-feldspar substantially affect porosity-permeability correlation in sandstone

### Correspondence to:

A. Kumar,  
akash.kumar@kit.edu

### Citation:

Kumar, A., Prajapati, N., Späth, M., Busch, B., Schneider, D., Hilgers, C., & Nestler, B. (2023). Qualitative dissolution modeling of etch-pit formation on the K-feldspar surface through phase-field approach. *Journal of Geophysical Research: Solid Earth*, 128, e2022JB025749. <https://doi.org/10.1029/2022JB025749>

Received 6 OCT 2022  
Accepted 28 MAR 2023

### Author Contributions:

**Conceptualization:** Akash Kumar, Nishant Prajapati, Michael Späth, Benjamin Busch, Christoph Hilgers, Britta Nestler  
**Data curation:** Akash Kumar  
**Formal analysis:** Akash Kumar  
**Funding acquisition:** Britta Nestler  
**Investigation:** Akash Kumar  
**Methodology:** Akash Kumar, Nishant Prajapati, Michael Späth, Christoph Hilgers, Britta Nestler  
**Project Administration:** Britta Nestler  
**Resources:** Benjamin Busch  
**Software:** Akash Kumar, Britta Nestler  
**Supervision:** Nishant Prajapati, Michael Späth, Daniel Schneider, Britta Nestler

© 2023. The Authors.

This is an open access article under the terms of the [Creative Commons Attribution-NonCommercial-NoDerivs License](https://creativecommons.org/licenses/by-nc-nd/4.0/), which permits use and distribution in any medium, provided the original work is properly cited, the use is non-commercial and no modifications or adaptations are made.

# Qualitative Dissolution Modeling of Etch-Pit Formation on the K-Feldspar Surface Through Phase-Field Approach

Akash Kumar<sup>1</sup> , Nishant Prajapati<sup>2</sup> , Michael Späth<sup>1</sup> , Benjamin Busch<sup>3</sup> , Daniel Schneider<sup>1,4</sup> , Christoph Hilgers<sup>3</sup> , and Britta Nestler<sup>1,2,4</sup> 

<sup>1</sup>Institute of Nanotechnology (INT), Karlsruhe Institute of Technology (KIT), Karlsruhe, Germany, <sup>2</sup>Institute for Applied Materials (IAM-MMS), Karlsruhe Institute of Technology (KIT), Karlsruhe, Germany, <sup>3</sup>Structural Geology and Tectonics, Institute of Applied Geosciences (AGW-SGT), Karlsruhe Institute of Technology, Karlsruhe, Germany, <sup>4</sup>Institute of Digital Materials Science (IDM), Karlsruhe University of Applied Sciences, Karlsruhe, Germany

**Abstract** Reservoir quality of sandstones can be controlled by the dissolution of minerals such as K-feldspar. The present work investigates the impact of dissolution of K-feldspar (Orthoclase) on the resulting porosity and permeability of sandstones using a thermodynamically consistent multiphase-field model. Two novel aspects of this research are: (a) identification and calibration of interfacial surface energy and kinetics related model parameters based on existing literature, to account for the formation and growth of diamond-shaped etch-pits during dissolution, and (b) the workflow for three-dimensional modeling of dissolution at sub-micrometer scale within individual feldspar grains, followed by up-scaling the phenomenon to a multigrain pack analogous to sandstone. The simulated dissolution, when visualized in the relevant planes, show clear similarities with microphotographs of natural samples and previous numerical works, in terms of facet-formation and merging of the etch-pit morphologies. For the computation of permeability, computational fluid dynamics analysis was performed for grain packs at different stages of dissolution. Finally, the generated data-sets were analyzed to study the impact of rock properties including a fraction of feldspar grains and their crystallographic orientation on the porosity, permeability and their correlations, for sandstones undergoing K-feldspar dissolution. At the same porosity, sandstones containing a greater proportion of K-feldspar grains are expected to have greater permeabilities. The devised workflow for model calibration and up-scaling complimented by the innovative post-processing and visualization techniques can be adapted to study dissolution of other minerals in different rocks.

**Plain Language Summary** The dissolution of minerals like K-feldspar controls how well sandstones act as a storage sites for fluids. In this work, we use a multi-physics modeling approach and perform simulations to study how K-feldspar grain dissolution impacts the overall porous and permeable characteristics of natural sandstones. The calibration of a simulation model helped us to capture the shape and growth characteristics of etch-pits, which are responsible for the dissolution of K-feldspar grains. Additionally, we perform pre- and post-processing techniques which allow the up-scaling of this phenomenon to a multigrain pack analogous to sandstone, while also reducing the computational costs. When comparing the simulation result with natural samples, the etch-pit's morphology evolution showcases great resemblance. Furthermore, for computation of the permeability evolution during K-feldspar grain dissolution, we performed computational fluid dynamics analysis. The fluid-flow analysis allows us to analyze the effect of the volume of K-feldspar grains and their respective cleavage plane (weaker plane, where etch-pits form) orientations on the overall porosity-permeability evolution within the sandstone. This work showcases new modeling techniques, which can be used in future work, for handling large-scale dissolution processes with different minerals and rock types.

## 1. Introduction

Sandstones are composed of various minerals, including quartz, feldspar, and other lithic fragments, and are among the most significant clastic geological reservoirs (Xiao et al., 2018). Geological processes, such as cementation and dissolution of minerals (e.g., quartz, carbonates, and feldspar) affect the reservoir quality, which is indicated by rock porosity and permeability (Doyen, 1988; Xiao et al., 2018; G. Yuan et al., 2019; Zhang et al., 2016). Depending on physical conditions, different minerals exhibit diverse dissolution behavior, resulting in different micromorphologies and physical properties. In the work of Trindade Pedrosa et al. (2019), various

**Validation:** Akash Kumar, Benjamin Busch

**Visualization:** Akash Kumar, Nishant Prajapati, Michael Späth, Benjamin Busch

**Writing – original draft:** Akash Kumar

**Writing – review & editing:** Akash Kumar, Nishant Prajapati, Michael Späth, Benjamin Busch, Daniel Schneider, Christoph Hilgers, Britta Nestler

surface microstructure's behaviors are investigated, which are the outcome of crystal characteristics. These behaviors (e.g., crystallographic orientation) can affect the dissolution rate and enable a better understanding of key characteristics involved during crystal dissolution. For instance, quartz grains exhibit faceted dissolution (Prajapati et al., 2021; Snyder & Doherty, 2007), while other minerals (such as calcite, feldspar, pyroxene) exhibit the formation and growth of “etch-pits” on the grain surface (Arvidson et al., 2003; Beig & Lüttge, 2006; Berner et al., 1980; Keith & Gilman, 1960; Lasaga & Lüttge, 2001; MacInnis & Brantley, 1992, 1993). Feldspar dissolution is an ubiquitous process occurring in sedimentary basins (Huang et al., 2003; Xiao et al., 2018), that facilitates the generation of secondary porosity, resulting in an increase of porosity and permeability, and thereby reservoir quality (Bjørlykke et al., 1988; Stoessell & Pittman, 1990; Surdam et al., 1984, 1989; Wilkinson et al., 2001; G. Yuan et al., 2015; X. Zhu et al., 2007). About one half of the volume of the earth's crust, is composed of feldspar minerals (Gout et al., 1997). Therefore, feldspar dissolution has been a topic of intensive research for geologists. Lange et al. (2021) for example, discussed the crystal heterogeneity and its major influence on the dissolution rate kinetics of alkali feldspar. This work demonstrates how the diverse chemistry and texture of the same set of feldspar crystals can result in different dissolution rate kinetics and provides a deeper understanding of the mechanical and chemical texture's function during the crystal dissolution. Furthermore, the etch-pit density and the temporal evolution of faceted etch-pitting on the surface of K-feldspar are evaluated in the experiments of Pollet-Villard, Daval, Ackerer, et al. (2016), which indicated that the prominent microstructural traits of K-feldspar (cleavage planes) accurately reflect their dissolution characteristics. Similar post-dissolution traits of K-feldspar are also observed in natural samples. Detrital feldspar grains often fracture along their cleavage during weathering, erosion, and transport. Since cleavage planes have a visible aperture even in recent unconsolidated sediments, the voids are easily filled by fluids, and etch-pits can emerge along those weaker planes.

Figure 1 showcases thin-section microphotographs of a sandstone sample with partially dissolved K-feldspar grains, as well as the orientation of the cleavage plane within these grains (black arrows, in Figures 1a–1c). Intragranular dissolution porosity is developed as prolonged etch-pits (red arrows in Figures 1b and 1c) along the K-feldspar grain's cleavage planes (black arrows). After, the etch-pitting of K-feldspar grains, the remaining elongated skeletal remnants of K-feldspar grains can be also seen in Figure 1 and have been also reported in other works, for example, G. Yuan et al. (2019); Pollet-Villard, Daval, Fritz, et al. (2016); Xiao et al. (2018); Kang et al. (2018); Hellmann and Tisserand (2005); Waldron et al. (1994); Liu et al. (2018). The contribution of dissolved feldspar grains to overall sandstone porosity by the generation of secondary pores has been quantified, for example, see the works of Lei et al. (2013); Baruch et al. (2015); Li et al. (2018); Xiao et al. (2018). However, its implications on the resulting permeability are difficult to estimate, as the generated pores may remain isolated (Pittman, 1979). Using digital rocks and novel modeling techniques (Monsees et al., 2020; Prajapati, Abad Gonzalez et al., 2020; Späth et al., 2021) one can assess the specific contribution of feldspar dissolution on permeability. Numerical modeling of geological processes has been playing a dominant role to gain insights, that are normally unavailable through laboratory experiments and field observations. Some of the works, such as of Zhang et al. (2016); Zhiyong et al. (2017); G. Yuan et al. (2019), have presented numerical models, that provide a reasonable approximation of the experimental results and provide insightful assessments of the porosity and permeability evolution as the feldspar grains dissolve inside the sandstone. In order to anticipate porosity and permeability in the future, understanding microstructural evolution dynamics is key. Numerical techniques that can reproduce the microstructure evolution within rock systems are useful to understand porosity and permeability can be seen in the works of Prajapati, Selzer, Nestler, Busch, Hilgers, et al. (2018) and Prajapati, Abad Gonzalez et al. (2020).

Different numerical approaches have been used to analyze mineral dissolution phenomenon in a diverse range of minerals (Lasaga & Lüttge, 2001; Pollet-Villard, Daval, Fritz, et al., 2016; Prajapati et al., 2021; Yang et al., 2021). Methods like, the *level-set method (LSM)* (Osher & Sethian, 1988) have been used to simulate mineral dissolution in porous systems (Ray et al., 2019; van Noorden, 2009). Lasaga and Lüttge (2001) demonstrated a *Monte Carlo simulation* for the creation of an etch-pit at the site of a dislocation defect and the production of dissolution step waves. Further, they showcased a *step-wave model* for controlling the bulk dissolution rate of feldspars. This approach implies dissolution occurs in separate steps or levels, and so it utilizes stepwaves at pit-walls to highlight the etch-pit profiles across the crystal surface. It has been extensively utilized during the last two decades to demonstrate the dissolution behavior of several mineral groups through etch-pitting (Bouissonnié et al., 2018; Kurganskaya et al., 2012; Pers et al., 2016; Schindler et al., 2011). This model can give insight to the connection between crystal lattice defects and the development of reactive surface sites, which drive the dissolution process.

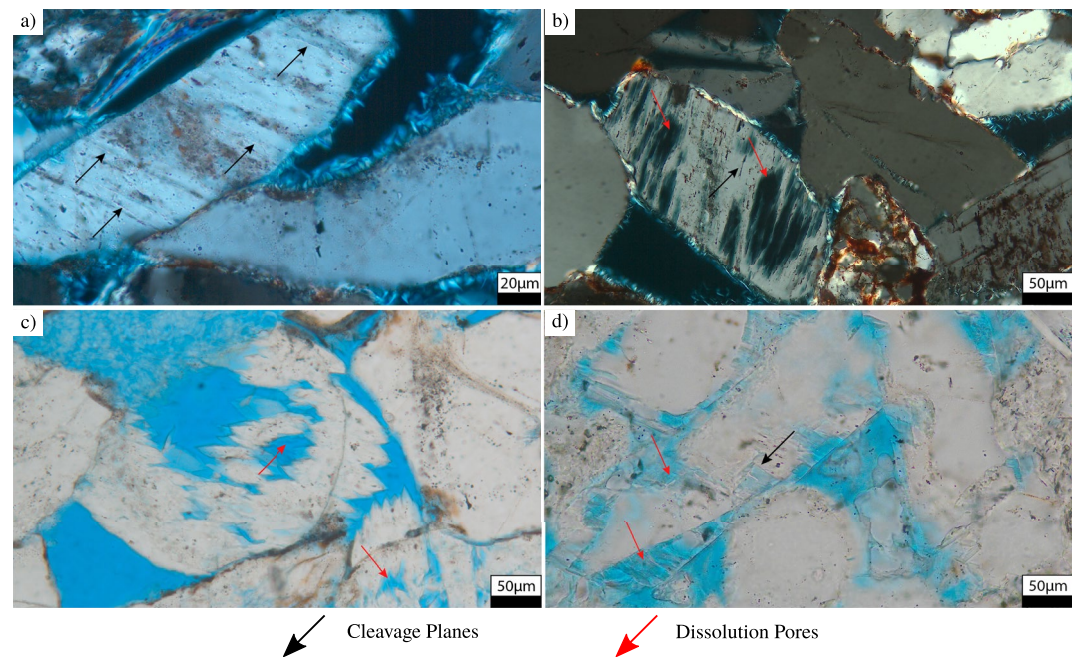


**Figure 1.** Thin section images highlighting cleavage planes (black arrows in a, b, and d) and intragranular dissolution pores in detrital K-feldspar grains (red arrows in b–d). All samples are retrieved from the Triassic Buntsandstein in southern Germany (see also Busch, Adelman, et al. (2022); Busch, Spitzner, et al. (2022)). (a, b) Under crossed and (c, d) under plane polarizers.

The dissolution process in nature does not produce perfectly smooth surfaces with etch-pits (Fischer et al., 2012; Lasaga & Lüttge, 2004). In contrast, dissolution results in the production of remarkably complex and rough topographies. Furthermore, the work of Fischer and Lüttge (2018), demonstrates that by including the pulsing impact of a stepwave (due to fluctuating stepwave velocity as it travels toward and away from etch-pit dislocations), the complex topography of an etch-pit can be adequately represented by this mathematical framework. Pollet-Villard, Daval, Ackerer, et al. (2016); Pollet-Villard, Daval, Fritz, et al. (2016) discussed a numerical technique to simulate K-feldspar dissolution in two dimensions (2D), based on several aspects such as chemical affinity, crystallographic orientations, and the varying reaction rate at different surfaces of K-feldspar grains. Other numerical modeling approaches, such as *discrete element method (DEM)*, *bonded-particle model (BPM)* (Sun et al., 2018), and *dynamic mesh framework* (K. Yuan et al., 2019), have been utilized to investigate mineral dissolution and its influence on the mechanical and chemical integrity of microstructures. Since the dissolution process of minerals affects the overall rock porosity and permeability at macroscale, a coupled micro-macro model using an up-scaling technique (Ray et al., 2019) has also been proposed, for the same. The research of Kurganskaya et al. (2023) discusses the modeling of crystal-liquid interaction at different scales (atomistic to meso-scale), in order to examine and comprehend various geological phenomena, including mineral dissolution. Except for the LSM, all the above-discussed numerical methodologies are based on the sharp-interface approach. Sharp interface approaches require complex numerical treatments such as explicit interface tracking and grid reconstruction at each time-step that incur further computational costs. In modeling moving boundary problems, diffuse interface approaches such as LSM and phase-field method (PFM) (Fix, 1982) serve as efficient numerical techniques, as they obviate the need to explicitly track the interfaces. In LSM, to maintain the prescribed distance function for tracking the change in the interface, a re-initialization step at every simulation time-step is required. The PFM controls the interface movement simply by updating the phase-field variable based on the evolution equation. Thus, unlike LSM, PFM does not require any kind of re-initialization (C.-S. Zhu et al., 2021).

PFM is a long established method in the material science community for modeling processes where interface motion occurs for example, phase-transition processes such as solidification and grain growth (L.-Q. Chen, 2002; Choudhury, 2017; Fix, 1982; Langer, 1980, 1986). The methodology has also emerged as a prominent computational method for modeling diverse geological processes, such as mineral cementation (Prajapati, Abad Gonzalez et al., 2020; Prajapati et al., 2017; Prajapati, Selzer, Nestler, Busch, Hilgers, et al., 2018),



fracture propagation in sandstone (Prajapati, Herrmann, et al., 2020), and formation of crack-seal morphologies such as quartz veins (Ankit et al., 2013; Ankit, Urai, & Nestler, 2015; Ankit, Selzer, et al., 2015; Späth et al., 2022a, 2022b; Wendler et al., 2016) and calcite veins (Prajapati, Selzer, Nestler, Busch, & Hilgers, 2018; Späth et al., 2021; Spruženiece et al., 2020, 2021). Further, mineral dissolution processes have been modeled using PFM in one dimension (1D) (Xu & Meakin, 2008) and two dimensions (2D) (Bringedal et al., 2020; Xu et al., 2012). Recently, Prajapati et al. (2021) proposed a generalized procedure of prescribing the anisotropies associated with the surface energy and particle detachment kinetics for the dissolving faceted crystals in two & three dimensions (2D & 3D). Some more interesting literature related to dissolution phenomenon within rock system can be found in the works of Yang et al. (2021); Xu and Meakin (2008); Bringedal et al. (2020). However, none of the above-mentioned PFM based works addressed the problem of etch-pitting processes that occur within individual grains.

The present work aims at 3D modeling the dissolution of K-feldspar grains along their cleavage planes in a sandstone matrix through the formation of etch-pits. Hereby, we adapt a multiphase-field model, and on the basis of an extensive literature review, determine the parameters that describe the anisotropies associated with the surface energy and particle detachment kinetics of the K-feldspar-water interface during etch-pitting dissolution. Furthermore, computational fluid dynamics (CFD) simulation is performed to compute the permeability of the numerically dissolved feldspar grains in sandstone packs at representative stages of time. Finally the generated numerical data sets were analyzed to study the implications of etch-pitting dissolution processes on the porosity, permeability, and their correlations on sandstone exhibiting different fractions of K-feldspar.

This article is structured as follows: Section 2 provides information about the sandstone sample containing K-feldspar grains, that is used as a reference sample for the present study. Section 3 elaborates the numerical modeling methods used in this work: (a) the equations of the multiphase-field model for K-feldspar dissolution (etch-pitting phenomenon), (b) prescription of novel modeling parameters, (c) modeling of quartz as inert phase, and finally (d) the equations related to fluid-flow simulations for computing permeability evolution. In Section 4, we present and elaborate our modeling and simulation results. As a starting point, in Section 4.1 we validate anisotropic modeling by recreating the etch-pitting morphologies found in previous numerical experiments (Pollet-Villard, Daval, Fritz, et al., 2016) and thin-section micro-photographs of reference natural samples. In Section 4.2, a novel workflow is presented for up-scaling the sub-microscale process of etch-pitting to sub-mm scale in a 3D multigrain system. The generated digital data sets for the feldspar dissolution are analyzed and the simulation results are discussed in detail in Section 4.3 and Section 4.4. Section 5 concludes the article by summarizing the key findings and inferences of this research work followed by an outlook on the scope for future directions.

## 2. Geological Background

Natural examples of intragranular porosity by feldspar dissolution were selected from the Triassic Buntsandstein (Induan-Olenekian) in southern Germany (see Busch, Adelman, et al. (2022); Busch, Spitzner, et al. (2022) for more detail). The samples have been selected since they do not feature pervasive replacements of K-feldspar by either kaolinite or illite, often reported in other siliciclastic samples (e.g., Lanson et al. (2002); Becker et al., 2019). Furthermore, illite and kaolinite formation predate the main phase of K-feldspar dissolution (Busch, Spitzner, et al. (2022)). While the average contribution of feldspar dissolution to the bulk rock volume of studied Buntsandstein samples is  $\sim 1.1\%$  (Busch, Adelman, et al. (2022)), its contribution to permeability cannot be clearly characterized.

## 3. Methods

This section describes the numerical method used in the current work. Section 3.1 outlines the equations for a generalized phase-field model of the mineral dissolution process. Next, we discuss the model adaption in the context of modeling K-feldspar dissolution along cleavage planes, and determine the parameter set in Section 3.2. In Section 3.3, we elaborate the numerical procedure for the treatment of quartz grains during the K-feldspar dissolution process. Finally, the equations corresponding to the fluid-flow model (for permeability calculations) are described in Section 3.4.

### 3.1. Phase-Field Model for K-Feldspar Dissolution

This section provides a summary of the multiphase-field model (based on the work of Nestler et al. (2005)) that is used to model the phenomena of K-feldspar dissolution caused by etch-pit formation. In a physical domain  $\Omega$  containing  $N$  phases  $\phi_\alpha$ , we consider,  $\boldsymbol{\phi}(\mathbf{x}, t) = [\phi_1(\mathbf{x}, t), \dots, \phi_N(\mathbf{x}, t)]$ . Each phase-field that is,  $\phi_\alpha : \Omega \times \mathbb{R}_0^+ \rightarrow [0, 1]$  describes the presence of certain phase  $\alpha \in [1, \dots, N]$  at  $\mathbf{x} \in \Omega$  and time  $t \in \mathbb{R}_0^+$ . The Helmholtz free energy  $\mathcal{F}$  of the system can be treated as the sum of the bulk and interfacial energy, and can be given by

$$\mathcal{F}(\boldsymbol{\phi}, \nabla \boldsymbol{\phi}) = \int_{\Omega} [f_{\text{bulk}}(\boldsymbol{\phi}) + f_{\text{intf.}}(\boldsymbol{\phi}, \nabla \boldsymbol{\phi})] d\Omega. \quad (1)$$

Here  $f_{\text{bulk}}(\boldsymbol{\phi})$  and  $f_{\text{intf.}}(\boldsymbol{\phi}, \nabla \boldsymbol{\phi})$  are the bulk and interface free energy densities respectively. The bulk energy density is given by

$$f_{\text{bulk}}(\boldsymbol{\phi}) = \sum_{\alpha=1}^N h^\alpha(\phi_\alpha) f_{\text{bulk}}^\alpha, \quad (2)$$

where  $f_{\text{bulk}}^\alpha$  is the phase-dependent free-energy density corresponding to phase  $\alpha$  and  $h^\alpha(\phi_\alpha)$  is an interpolation function. During the dissolution process, the liquid phase free energy density is set to zero and the solid phase free energy density to a non-zero value, which results in a driving force for the solid-liquid interface. The interfacial energy density contributions are expressed by

$$f_{\text{intf.}}(\boldsymbol{\phi}, \nabla \boldsymbol{\phi}) = \epsilon a(\boldsymbol{\phi}, \nabla \boldsymbol{\phi}) + \frac{1}{\epsilon} \omega(\boldsymbol{\phi}), \quad (3)$$

where the first term  $\epsilon a(\boldsymbol{\phi}, \nabla \boldsymbol{\phi})$  refers to the gradient energy density and the second term  $\omega(\boldsymbol{\phi})/\epsilon$  denotes the potential energy density.  $\epsilon$  is a length scale parameter that controls the width of the diffuse interface. The length scale parameter should be set to a value that resolves the interface with good amount of cells (grid points). The multi-obstacle type potential is given by

$$\frac{1}{\epsilon} \omega(\boldsymbol{\phi}) = \begin{cases} \frac{16}{\epsilon \pi^2} \sum_{\substack{\alpha, \beta=1 \\ (\alpha < \beta)}}^{N, N} \gamma_{\alpha\beta} \phi_\alpha \phi_\beta + \frac{1}{\epsilon} \sum_{\substack{\alpha, \beta, \delta=1 \\ (\alpha < \beta < \delta)}}^{N, N, N} \gamma_{\alpha\beta\delta} \phi_\alpha \phi_\beta \phi_\delta & , \text{ if } \boldsymbol{\phi} \in \mathcal{G} \\ \infty & , \text{ else,} \end{cases} \quad (4)$$

where the Gibbs simplex,  $\mathcal{G} = \boldsymbol{\phi} \in \mathbb{R}^N | \left( \sum_{\alpha=1}^N \phi_\alpha = 1 \text{ and } \phi_\alpha \geq 0 \right)$  ensures the summation constraint. The second sum in Equation 4 avoids spurious phases occur in binary interface regions (see, Nestler et al., 2005). Here,  $\gamma_{\alpha\beta}$  denotes the  $\alpha - \beta$  interfacial energy density. The choice of multi-obstacle potential reduces the computational costs, since the phase-field evolution equations (Equation 6) only need to be updated in the gradient regions, rather than the entire simulation domain. The gradient energy density is expressed by

$$\epsilon a(\boldsymbol{\phi}, \nabla \boldsymbol{\phi}) = \epsilon \sum_{\substack{\alpha, \beta=1 \\ \alpha < \beta}}^{N, N} \gamma_{\alpha\beta} \left[ a_{\alpha\beta}^{\text{cap}}(\mathbf{n}_{\alpha\beta}) \right]^2 |\mathbf{q}_{\alpha\beta}|^2, \quad (5)$$

where  $\mathbf{q}_{\alpha\beta} = \boldsymbol{\phi}_\alpha \nabla \boldsymbol{\phi}_\beta - \boldsymbol{\phi}_\beta \nabla \boldsymbol{\phi}_\alpha$  is the normal vector of the  $\alpha - \beta$  interface and  $\mathbf{n}_{\alpha\beta} = \mathbf{q}_{\alpha\beta} / |\mathbf{q}_{\alpha\beta}|$  is the corresponding normalized unit vector in the same direction. The surface energy of the  $\alpha - \beta$  interface can be modeled anisotropically by the function  $a_{\alpha\beta}^{\text{cap}}(\mathbf{n}_{\alpha\beta})$ . In Section 3.2 we address the choice of the capillary anisotropy function and the prescription of input variables in the perspective of modeling faceted etch-pits (primarily for the dissolution of K-feldspar). The evolution equation for each phase ( $\phi_\alpha$ ) is determined by the variational derivation of the energy functional, that is,

$$\epsilon \frac{\partial \phi_\alpha}{\partial t} = \mu(\boldsymbol{\phi}, \nabla \boldsymbol{\phi}) \left( -\frac{\delta \mathcal{F}}{\delta \phi_\alpha} - \lambda \right). \quad (6)$$

This equation assures that the free-energy drops monotonically with time. The interfacial kinetics are regulated by the mobility  $\mu(\boldsymbol{\phi}, \nabla \boldsymbol{\phi})$ , and the lagrange multiplier ( $\lambda$ ) guarantees that  $\sum_{\alpha=1}^N \phi_\alpha = 1$  is maintained at each

computational grid point. Additionally, substituting Equation (1) into Equation 6 results in the partial differential equation

$$\epsilon \frac{\partial \phi_\alpha}{\partial t} = \mu(\phi, \nabla \phi) \left[ \overbrace{-\frac{\partial f_{\text{bulk}}}{\partial \phi_\alpha} + \epsilon \left( \nabla \cdot \frac{\partial a(\phi, \nabla \phi)}{\partial \nabla \phi_\alpha} - \frac{\partial a(\phi, \nabla \phi)}{\partial \nabla \phi_\alpha} \right)}^{\text{rhs}_\alpha} - \frac{1}{\epsilon} \frac{\partial \omega(\phi)}{\partial \phi_\alpha} - \lambda \right] \text{ for } \alpha = 1 \dots N, \quad (7)$$

where,

$$\lambda = \frac{\sum_{\alpha=1}^N \text{rhs}_\alpha}{N}.$$

Also, the kinetic mobility  $\mu(\phi, \nabla \phi)$  is calculated with

$$\mu(\phi, \nabla \phi) = \frac{\sum_{\substack{\alpha, \beta=1 \\ \alpha < \beta}}^{N, N} \mu_{\alpha\beta}^0 a_{\alpha\beta}^{\text{kin}}(\mathbf{n}_{\alpha\beta})}{\sum_{\substack{\alpha, \beta=1 \\ \alpha < \beta}}^{N, N} \phi_\alpha \phi_\beta},$$

where  $\mu_{\alpha\beta}^0$  denotes the kinetic mobility coefficient of the  $\alpha - \beta$  interface, and the  $a_{\alpha\beta}^{\text{kin}}(\mathbf{n}_{\alpha\beta})$  represents the scalar-valued kinetic anisotropy function that regulates the dissolution direction kinetics.

Anisotropy functions for surface energy and kinetic anisotropy are described in Section 3.2 in relation to faceted etch-pit dissolution of K-feldspar grains. PACE3D (Hötzer et al., 2018), a parallel multi-physics computing environment based on the C programming language, is used to implement the model equations in this work. The phase-field evolution equation is solved using a forward Euler scheme for the temporal derivative and a second-order accurate central difference scheme for the spatial derivatives. Since the present model does not account for solute concentration, the existing mathematical framework does not account for characteristics such as, advective and diffusive solute mass transfer in the fluid. In addition, the positioning of spherical etch-pits on the surface of K-feldspar grains was random, since it was considered that etch-pits grow along the grain's weaker cleavage planes, that are randomly oriented in nature. The simulation parameters for the simulation of the etch-pit evolution in K-feldspar grains are chosen in order to obtain a numerically stable simulation, while reducing the computational costs. The parameters are given in Table 1 as non-dimensional values. K-feldspar dissolution is strongly dependent on the environment (alkaline or acidic) (Xiao et al., 2018; G. Yuan et al., 2019). The dissolution process of K-feldspar generates different by-products at different physical conditions (based on temperature and pH), so finding all the required data

for a certain experimental data set (at specific temperature, concentration, and pH) and performing a quantitative analysis is difficult. Some investigations, such as that of Gautier et al. (1994), have used controlled environments for their experiments, but unless the parameters of the fundamental physical reaction are known, a quantitative analysis cannot be accomplished.

### 3.2. Modeling Faceted Etch-Pitting

In the experimental work by Pollet-Villard, Daval, Fritz, et al. (2016), the formation of symmetric diamond-shaped etch-pits on (001) surfaces (cleavage plane) of K-feldspar was described, along with their characteristics such as Miller indices of the pit edges and angle between them. In order to describe the formation of faceted etch-pits, we choose a crystalline anisotropy for the surface energy of the following form

$$a_{\alpha\beta}^{\text{cap}} = \max_k \{ \mathbf{n}_{\alpha\beta} \cdot \boldsymbol{\eta}_k^{\text{cap}} \} \quad \text{for } k = 1, \dots, N_{\text{cap}}. \quad (8)$$

**Table 1**  
Non-Dimensional Values of the Numerical Parameters Used for the Phase-Field Simulations

Model parameter	Symbol	Nondim. Value
Grid cell size	$\Delta x$	1.0
Time-step width	$\Delta t$	0.1
$\alpha - \beta$ interfacial energy density	$\gamma_{\alpha\beta}$	1.0
Higher-order parameter	$\gamma_{\alpha\beta\delta}$	15
Length scale parameter	$\epsilon$	4.0
Kinetic coefficient of the $\alpha - \beta$ interface	$\mu_{\alpha\beta}^0$	1.0
Bulk energy density (feldspar)	$f_{\text{feldspar}}$	-0.3
Bulk energy density (liquid)	$f_{\text{liquid}}$	0.0

Here, the function  $\max_k(\dots)$  returns the largest argument of the dot products between the interface normal unit vector  $\mathbf{n}_{\alpha\beta}$  and the vertex vectors of the capillary shape  $\boldsymbol{\eta}_k^{cap}$ . The  $N_{cap}$  vertex vectors are assembled in the tuple  $\mathcal{N}^{cap} = \{\boldsymbol{\eta}_1^{cap}, \dots, \boldsymbol{\eta}_{N_{cap}}^{cap}\}$ , which is determined based on the target faceted morphology (i.e., etch-pits). Capillary anisotropy controls the form of pits due to the minimization of surface energy under diminishing driving forces. In the same experiment, it was found that the etch-pits evolve 10 times faster in the *in-plane* direction than in the direction perpendicular to the cleavage planes (discussed in detail in Section 4.1). In order to model direction dependent particle detachment kinetics, we chose a similar form for the kinetic anisotropy function as follows

$$a_{\alpha\beta}^{kin} = \max_k \{ \mathbf{n}_{\alpha\beta} \cdot \boldsymbol{\eta}_k^{kin} \} \quad \text{for } k = 1, \dots, N_{kin}, \quad (9)$$

where  $\mathbf{n}_{\alpha\beta}$  represents the unit phase-field gradient vector.  $\boldsymbol{\eta}_k^{kin}$  represents the  $k$ th member of the set  $\mathcal{N}^{kin} = \{\boldsymbol{\eta}_1^{kin}, \dots, \boldsymbol{\eta}_{N_{kin}}^{kin}\}$  of  $N_{kin}$  geometric vectors, that are determined through simulations presented in Section 4.1, by recreating the desired shift velocity of different facets of the etch-pits.

### 3.2.1. Anisotropy Parameters for an Etch-Pit Morphology (K-Feldspar Dissolution)

According to work of Pollet-Villard, Daval, Fritz, et al. (2016), K-feldspar dissolution occurs far more rapidly along the cleavage planes than on the facets itself. This tendency may be attributed to the weak bonding of atoms along cleavage planes and the presence of micro-fluid inclusions inside these planes. In the microphotographs shown in Figure 1, etch-pit morphologies clearly illustrate that pit growth occurs at faster rate along the cleavage plane (parallel to those planes) than in the direction perpendicular to them. The authors of above-mentioned work determined the beginning and growth forms of pits, generated on the (001) surface of K-feldspar. Specifically, these pits were constructed in the form of a diamond, with facets aligned at varying angles. The diagonals of this diamond-shaped pit were perpendicular to the [100] & [010] axes. The angle between two consecutive facets of pits was found to be  $63 \pm 5^\circ$  and  $121 \pm 5^\circ$ , while the angle between the (001) surface and facets of the pit was determined to be  $27 \pm 5^\circ$ . Additionally, they found that the etch-pit forms facets with the following Miller indices: (656), (656), (6511) and (6511), as also illustrated in Figure 2. Based on the information about the facets and their growth rates presented in the work of Pollet-Villard, Daval, Fritz, et al. (2016), we determine the anisotropy parameters for our multiphase-field model related to etch-pits in the following sub-sections:

### 3.2.2. Input Parameters for Capillary Anisotropy Function

Figure 2a depicts the capillary shape of the etch-pit, where the angles between the facets ((656),  $\bar{(656)}$ ,  $\bar{(6511)}$  &  $(6511)$ ) and the (001) surface are consistent with the findings of Pollet-Villard, Daval, Fritz, et al. (2016). Further, the symmetry along the (001) plane was ensured. The corresponding input set of vertex vectors is listed in Table A1 (see Appendix A). The resulting 3D polar plot of the surface energy is displayed in Figure 2b. The corresponding 2D shape (projection in (001) plane) as utilized for the 2D simulations, along with the 2D polar plot are depicted in Figure 2c.

### 3.2.3. Input Parameters for the Kinetic Anisotropy Function

The experiments of Pollet-Villard, Daval, Fritz, et al. (2016) shows the dissolution along an (100) plane is 10 times faster than perpendicular to it. We model different relative shift velocities of facets by incorporating an anisotropic kinetic mobility. The kinetic anisotropy shape is chosen to exhibit the same facets as the capillary shape, but differing normal distance from the geometric center, see Figure 2d. The kinetic anisotropy shape vectors are calibrated through numerical experiments of a single pit growth in 3D, which is present in Section 4.1, and recreating the observations of Pollet-Villard, Daval, Fritz, et al. (2016). The determined set of vertex vectors for the kinetic anisotropy are given in Table A2 (see Appendix A). The resulting 3D polar plot of the kinetic mobility is shown in Figure 2e. The 2D projection (along the (001) plane) and the corresponding 2D polar mobility plot are depicted in Figure 2f.

## 3.3. Modeling Quartz Grains as Inert Phases

As our work focuses on modeling the etch-pit dissolution of K-feldspar grains in sandstones, we require numerical treatment for the existence of quartz in the multigrain system. The works of Anbeek et al. (1994); Sokolova (2013); X. Chen et al. (2015) report that the dissolution rates of feldspar are orders of magnitude higher than that of quartz. Therefore, we assume quartz grains as an inert phases in our modeling. This numerical treatment is incorporated by solving the model equations according to the updated free energy functional given by

$$\mathcal{F}(\phi, \nabla\phi) = \int_{\Omega - \Omega_q} [f_{\text{bulk}}(\phi) + f_{\text{intf}}(\phi, \nabla\phi)] d\Omega,$$

where  $\Omega_q$  is the domain volumes for the inert quartz grain. A similar methodology has been utilized by Ankit, Selzer, et al. (2015) for modeling other inert phases in their numerical investigations.

### 3.4. Permeability Calculation During Different Dissolution Stages

In order to compute the permeability of the sandstone packs with numerically dissolved feldspar grains at different stages of time, CFD analysis is utilized. We use Stokes equations, according to the assumptions of laminar flow (i.e.,  $Re \ll 1$ ) within the porous sandstone, as follows:

$$\begin{aligned} \mu_d \Delta \mathbf{u} - \nabla p &= \mathbf{0}, \\ \nabla \cdot \mathbf{u} &= \mathbf{0}. \end{aligned}$$

Here  $\mu_d$  denotes the dynamic viscosity,  $\mathbf{u}$  signifies the fluid flow velocity, and  $\nabla p$  is the pressure gradient. Using a constant-pressure boundary condition, the velocity field is calculated. The  $x$ -direction boundaries of our domain are set to a constant pressure difference, which serves to govern the flow in the same direction, while all other boundaries are set to a slip boundary condition (Figure 9). The contact between the liquid and grain systems has a no-slip boundary condition, which is denoted by,  $\mathbf{u}|_{\text{interface}} = \mathbf{0}$ . The permeability  $k$  is calculated by the Darcy's law:

$$k = \frac{\mu_d \bar{v}}{\Delta p / \Delta x}, \quad (10)$$

where  $\bar{v}$  denotes the mean velocity of fluid.

## 4. Results and Discussion

In this section, we showcase our simulation results and present a detailed analysis of the generated data sets. As a starting point, in Section 4.1 we calibrate and validate the model to capture the growth tendencies and morphologies of the etch-pits based on the work of Pollet-Villard, Daval, Fritz, et al. (2016). In Section 4.2, we present a three-step work flow, devised for up-scaling the simulation of the submicroscopic phenomenon of etch-pitting to the sub-mm scale of a grain pack (analogous to quartz sandstone containing certain amount of K-feldspar grains). The workflow is demonstrated by considering a 2D numerical thin-section of a sandstone, and simulating the etch-pitting in it. Next, simulation studies in 3D grain packs are performed, and the simulated etch-pitting in one of the 3D grain pack is showcased and compared with the natural samples in Section 4.3. Finally, based on the generated data sets through simulation studies, the implications of etch-pitting on the porosity, permeability and their correlations for different grain packs with varying fractions and crystallographic orientation of K-feldspar grains are discussed in Section 4.4.

### 4.1. Model Calibration and Validation

#### 4.1.1. Single Etch-Pit Growth

We consider a cuboidal domain of size,  $100\Delta x \times 300\Delta x \times 100\Delta x$  (with  $\Delta x = 1 \mu\text{m}$ ), filled with a K-feldspar grain, and a small spherical pit (liquid phase) in the center, see Figure 3a at the initial stage. For the sake for visualization, only the etch-pit is shown. We incorporated the capillary anisotropy parameters given in Table A1 (see Appendix A), corresponding to the diamond-shaped pit morphology (see Section 3.2). Further, the set of input vertex vectors for kinetic anisotropy shape, listed in Table A2 (see Appendix A), was calibrated to recover the known relative growth rates of etch-pit facets (Pollet-Villard, Daval, Fritz, et al., 2016). Figure 3a depicts the different stages of the pit growth. As the pit grows, flat facets corresponding to the capillary anisotropy shape are formed. Different facets of the pit grow at different rates based on the calibrated parameters, resulting in a flat diamond-shaped morphology. Figure 3b depicts a plot of calibrated relative velocities of distinct etch-pit's facets along different growth directions (as indicated in Figures 3c and 3d, that are computed using the work of Pollet-Villard, Daval, Fritz, et al. (2016)). Our calibrated model captures the correct facet formation and their



relative growth rates. In nature, however, reaction rates in closed geochemical systems without a regular replenishment of undersaturated water would likely be slower.

#### 4.1.2. Multiple Etch-Pit Growth in a 2D Section

Here, we apply the calibrated model in a two-dimensional domain ( $600\Delta x \times 600\Delta x \times 1\Delta x$ , with  $\Delta x = 1\ \mu\text{m}$ ) using similar setup as in the work of Pollet-Villard, Daval, Fritz, et al. (2016), in order to test our modeling approach in a more complex environment. Also, Figure 4 compares the outcomes of our simulation approach with the findings of Pollet-Villard, Daval, Fritz, et al. (2016) and shows good resemblance. In Figure 4, successive phases of pit development, along with its characteristics such as, directional growth rate and relevant facet formation are shown in a two-dimensional section, beginning with the nucleation of pits as point defects (on the K-feldspar surface) at the initial stage of dissolution. As the time proceeds, the pits on the surface of K-feldspar acquire faceted forms, and continue to grow. Eventually, all of the faceted etch-pits combine and dissolve the surface of the K-feldspar mineral.

As the objective of this research is not only to analyze the evolution of etch-pit morphology, but also to comprehend the impact of K-feldspar grain dissolution on the overall porosity and permeability of the sandstone, it is necessary to conduct a complex and extensive three-dimensional simulation. These huge simulations can be computationally expensive, and thus an efficient computational workflow to overcome this is introduced later in this study (see, Section 4.2). Additionally, the same novel workflow will be implemented in the three-dimensional domain, and the subsequent outcomes will be presented in Section 4.3.

#### 4.2. Modeling Etch-Pitting of K-Feldspar Grains in Sandstone

In the previous section, we validated our model and found that it agrees well with literature. In the next step, we introduce the novel workflow to model the etch-pitting of K-feldspar along its cleavage planes within the natural sandstone (see Figure 1). As mentioned in Section 3.1, the etch-pits were randomly distributed across the surface of the K-feldspar grain, with the random orientation of the grain's weaker cleavage planes being the leading factor. Furthermore, we can examine the development of porosity over time using this study, and we can also perform permeability analyses to show how fluid connectivity evolves (see Section 4.4). Microscopic examination of sandstone thin-section shows that these pits can be as small as  $10 - 50\ \mu\text{m}$  in diameter, and are found on cleavage planes of K-feldspar grains (which are as large as  $300 - 500\ \mu\text{m}$  in diameter) and cause the dissolution of these grains. Before proceeding with the simulation analysis, it is critical to recognize the main obstacles that may arise during the computational investigations. Listed below are the two most significant obstacles we encountered during numerical evaluation, as well as an explanation of the need to implement a novel simulation methodology:

1. First, it is crucial to resolve the tiny etch-pit's growth morphology inside a relative large sandstone structure. If these small pits are directly embedded into the tenfold larger K-feldspar grains, which are present inside the  $10^3$  times larger sandstone sample, then the length scale ( $\Delta x$ ) will be too small to capture the pit evolution that it will be unable to highlight the difference of bulk and diffuse interfaces between pit and K-feldspar grains, thus violating the phase-field approach and leading to poor simulation studies. In order to overcome this, a workflow (see Figure 5) has been crafted for recording the pit's diffuse and bulk interface evolution over time.
2. The second major obstacle is the nucleation of pits on K-feldspar grains using only a single fluid phase with a single supersaturation state in regard to the dissolving phase. Experimental data suggests that fluids in smaller pore spaces can maintain higher supersaturations than fluids in larger pore spaces (e.g., Emmanuel & Berkowitz 2007; Rijniers et al., 2005). Given the etch-pit localization along cleavage planes within K-feldspar grains, it is possible that the thin fluid films along cleavage planes can maintain higher supersaturations and can form etch-pits. At the same time the outside of the K-feldspar grain remains unaltered as the solubility in the fluid filling the intergranular pore volume is lower. This analogy helps us to include the secondary liquid phase (more undersaturated liquid phase) into our simulation model, resulting in the growth of etch-pits (see in Figure 5f). In addition, we remark that the current simulation model is capable of displaying the phase evolution using a constant driving force. The assumption of constant driving force indicates that the fluid is continually replenished, resulting in a constant solute concentration within the system. The fundamental objective of the presented study (i.e., visualization of the evolution of etch-pit morphology on the surface of K-feldspar grains) can be attained without taking solute concentration evolution into consideration. In order to reduce the complexity of our simulation analysis and to decrease computational costs, we did not account for the solute concentration in this work. Nevertheless, with the suitable data-sets and model adaptations, it can be considered in future works to give more detailed insights.

In Figure 5a, a multigrain sandstone is considered (adapted from the work of Prajapati, Abad Gonzalez et al. (2020)), and to limit computational cost, a small three-dimensional section is then extracted out of it (Figure 5b). For the 2D simulations, we additionally cut out a slice from the 3D section to further reduce computational time (Figure 5c). Different studies and works (such as, Long (2017); Dong et al. (2019); Xiao et al. (2018); G. Yuan, Cao, Gluyas, et al. (2015)), indicate that the amount of K-feldspar grains can vary a lot based on locations as a function of the sandstone's provenance and other physical conditions, ranging from ~6% to 12.5%. This study considers ~7.2% of grains as K-feldspar grains (highlighted in Figure 5d) within the considered sandstone, while the remaining grains are classified as quartz grains. Furthermore, each K-feldspar grain (as specified in Figure 5e) is resolved four times larger than its original resolution for capturing and visualizing the pitting phenomenon more distinctively. Additionally, the secondary liquid phase is introduced around the weaker edges of K-feldspar grains, depending on the orientation of cleavage planes to induce the nucleation and evolution of etch-pits (as shown in Figure 5f). Finally, after complete dissolution of each K-feldspar grain, they are resolved to their original resolution and integrated back into its original position within the grain pack using post-processing techniques (Figure 5g). Foremost, we implement our novel workflow to investigate etch-pit formation in a 2D numerical setup ( $7243\Delta x \times 8683\Delta x \times 1\Delta x$ , with  $\Delta x = 1 \mu\text{m}$ ), where all the essential characteristics of etch-pitting can be demonstrated (Figure 6). Later, we extend this approach to 3D to demonstrate fluid connectivity evolution within sandstone due to K-feldspar dissolution. Previous investigations demonstrated strong agreement with 2D simulation studies, but they were unable to capture the fluid-connectivity evolution and the influence of variably oriented cleavage planes in all of the three dimensions. Thus, a 3D simulation research can enable us to demonstrate the aforementioned unaddressed points. In Figure 6, the evolution of the pit's morphology is illustrated at various simulation time-steps. We observe, that, the dissolution along the cleavage plane is much faster (according to the calibration), formation of different pit's facets, dissolution perpendicular to the cleavage plane is slower until different pits annihilate and then K-feldspar grains fully dissolve. Essentially, our analysis demonstrated how the expansion of etch-pits gradually merge into one another, resulting in the generation of more extensive inter-connecting micro fluid channels and ultimately enhancing the grain pack's total porosity.

### 4.3. Dissolution of K-Feldspar Grains in 3D Digital Sandstone

Following completing the 2D simulation, the 3D simulation is needed to examine the permeability evolution within sandstone due to K-feldspar dissolution. The numerical sandstone structure in this research with dimensions ( $799\Delta x \times 699\Delta x \times 494\Delta x$ , with  $\Delta x = 1 \mu\text{m}$ ) consists of 7.25 vol% of the overall sandstone and have a random crystallographic orientation (relative to the  $z$ -axis in a 3D-coordinate system) with an initial porosity of 10.23%. The digital sandstone pack consists total of 537 grains (including both quartz and feldspar grains), with an average grain size of approximately  $96 \mu\text{m}$ . Before running this computationally intensive simulation, it's crucial to understand the problem's scale. Since these grains are micrometer-sized, the pits along their cleavage planes are almost 10 times smaller in scale. A similar method to Section 4.2 is used to run the 3D simulation. Figure 7 shows how grains are segregated from the original multigrain pack and dissolved through etch-pits nucleation on the same. The phase-field simulations of the dissolution of K-feldspar grains in sandstone exhibits visibly good agreement to dissolution phenomena occurring within natural sandstone (as can be seen from Figure 8). Figures 8b and 8c, depicts a comparison between experimental images and the simulation-based results, where one can see, that the pit nucleation occurs on a range of different planes, in a diverse array of orientations, and in multitude of sizes. Eventually, the etch-pitting phenomena annihilates the whole K-feldspar skeletal framework.

### 4.4. Implication on the Porosity and Permeability Evolution During K-Feldspar Dissolution

Since K-feldspar grains dissolve way faster than quartz (see, Section 3.3), we aim to conduct crucial simulation-based experiments to determine how its dissolution affects sandstone porosity and permeability. Here, we analyze the fluid connectivity of the numerical sandstone in intermediate dissolution stages of K-feldspar grains and calculate the evolution of porosity-permeability relationship using Darcy's law (see Equation 3.4). The initial porosity of the sandstone used for this simulation experiment is  $\approx 10.23\%$ . The dimension of the digital sandstone is ( $799\Delta x \times 699\Delta x \times 494\Delta x$ ), where  $\Delta x = 1 \mu\text{m}$  (same as mentioned in Section 4.2 & Section 4.3).

Figure 9a–9d shows fluid streamlines in sandstone at different phases of K-feldspar grain dissolution. Fluid first flows via open pores, but as dissolution occurs, pore density rises, forming new flow connections and locally increasing flow connectivity. Flow connectivity may improve once all K-feldspar grains dissolve (depending on the existing location of fluid channels within a sandstone). And as predicted by previous research works

**Table 2**  
Non-Dimensional Values of the Parameters Used for CFD Analysis and Permeability Computation

Parameters	Symbol	Non-dim. value
Pressure gradient	$\Delta p$	2.0
Dynamic viscosity	$\mu_d$	0.9087
Fluid Density	$\rho$	1.0

(Bjørlykke et al., 1988; Stoessel & Pittman, 1990; Surdam et al., 1984, 1989; Wilkinson et al., 2001; G. Yuan et al., 2015; X. Zhu et al., 2007), the dissolution of K-feldspar grains in a sandstone should increase porosity and permeability of the pack. The evolution of both quantities, porosity and permeability are determined from the simulation data and displayed in Figure 9e). Here, it is evident that the dissolution of selected K-feldspar grains (7.25% by volume of the overall grain pack) has a noticeable impact on the progression of the sandstone's overall porosity and permeability evolution. The selected non-dimensional parameters for this fluid-flow study are shown in Table 2.

We investigate two different cases in this work, (a) the effect of the proportion of dissolving K-feldspar grains (see Section 4.4.1), and (b) the influence of K-feldspar grain's orientation (see Section 4.4.2).

#### 4.4.1. Influence of Percentage of K-Feldspar Grains

As etch-pits nucleate along K-feldspar cleavage planes, porosity rises very slightly. Nevertheless, as time passes, additional etch-pits nucleate and develop along the grain's cleavage planes, causing porosity to increase progressively in the sandstone (Figure 9e). When grains dissolve along the cleavage plane during the initial stage of dissolution, permeability doesn't increase rapidly. Once fluid connectivity is achieved, the permeability shows a linear increment, starting after the 2,000 simulation time-step and continues till the 6,000 simulation time-step. After the 8,000 simulation time-step (as soon as fluid connectivity is attained), permeability does not rise significantly, but porosity grows until all K-feldspar grains are fully dissolved (Figure 9e).

In this section, we explored the response of varying number of K-feldspar grains (5.1% and 7.3%) and noticed that permeability and porosity rises once the etch-pits began to develop. As more grains can potentially be dissolved, an increase in pore volume and permeability can be noticed (Figure 10a).

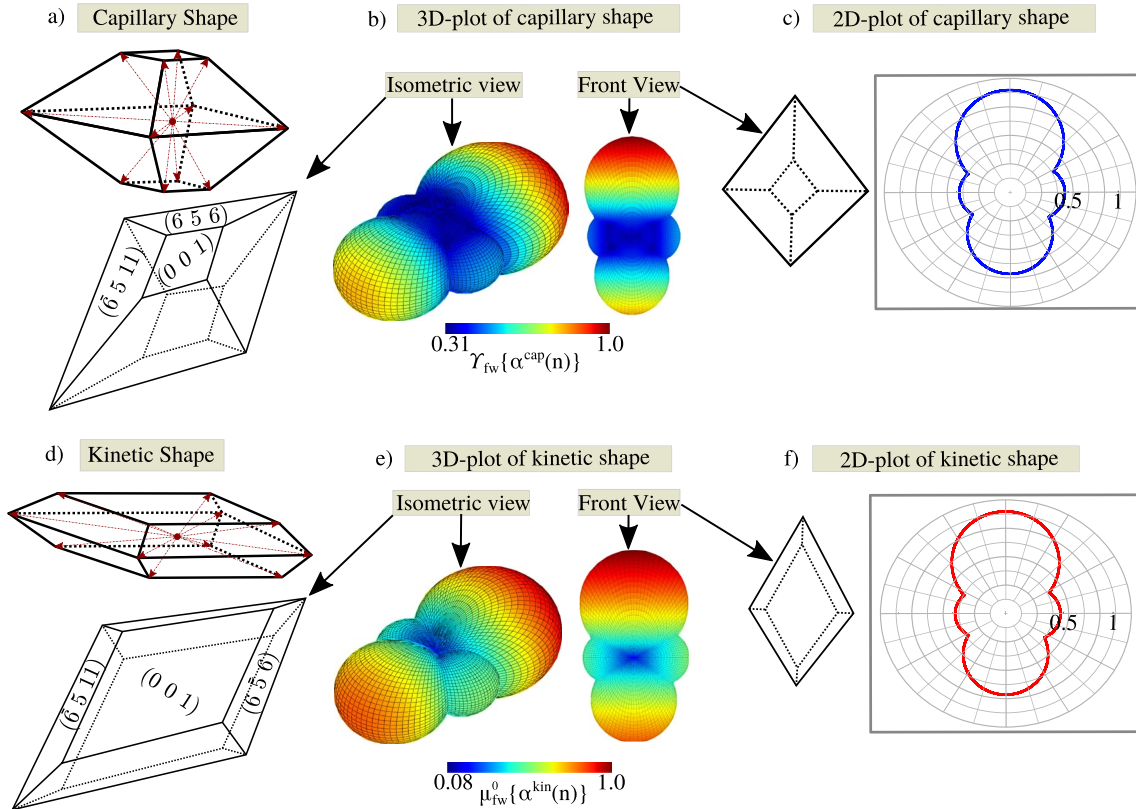


**Figure 2.** Crystallographic shapes of etch-pits which form during dissolution, and are used in the phase-field simulations. (a) Resulting capillary shape of etch-pit, after numerical modeling. (b) Surface energy plot of the resulting shape (Isometric & Front view). (c) 2D projection of the surface energy plot. (d) Resulting kinetic shape of etch-pit, after numerical modeling. (e) Kinetic energy plot of the resulting shape (Isometric & Front view). (f) 2D projection of the kinetic energy plot.

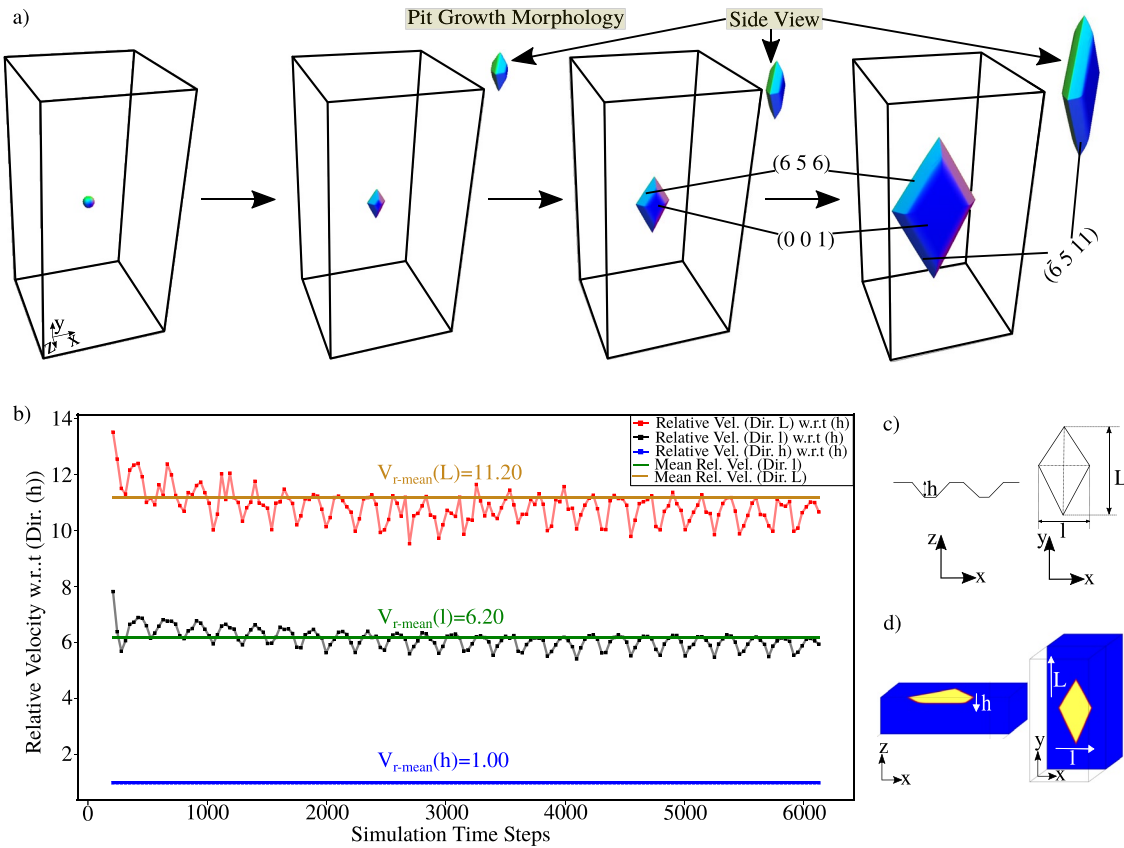


**Figure 3.** (a) Evolution of an etch-pit, showing different resulting facets at different simulation stages. (b) Relative ( $v/v_h$ ) & mean relative velocity ( $v_m$ ) of a single etch-pit (facet) along x- (l), y- (L), & z- (h) directions with respect to direction (h). (c) Schematic illustration of distinct facets growth trajectory (l, L, & h) in 2D. (d) 3D cross-sectional view of final stage simulation (as shown in a), showcasing the different growth trajectories (similar as in c).

#### 4.4.2. Influence of Crystal Orientations

This section examines how the crystallographic orientation of K-feldspar influences the permeability-porosity relation. In this section, we altered the orientation of K-feldspar grains (along z-axis). We focused on the following three orientation states of K-feldspar grains:

- *Parallel to the direction of fluid-flow:* When the etch-pit development in all K-feldspar grains arises parallel to the direction of flow ( $0^\circ$  w.r.t z-axis), causing the least potential obstruction to the fluid flow.
- *Orthogonal to the direction of fluid-flow:* When the etch-pit development in all K-feldspar grains evolves orthogonal to the direction of flow ( $90^\circ$  w.r.t z-axis), hence causing the greatest potential obstruction to the fluid flow.
- *Random:* Any possible crystallographic arrangement that falls between the parallel and orthogonal orientation states is considered to be random.

We set the length scale to  $\Delta x = 1 \mu\text{m}$  for this numerical analysis and plot the permeability as a dimensional quantity with the unit *milli Darcy* (mD) ( $1 \text{ mD} = 9.869233 \times 10^{-16} \text{ m}^2$ ) (Figure 10). In the first case, when etch-pits evolve parallel to the direction of flow (here along the x-axis), we observe a stronger increase of the permeability compared to the second case where the etch-pits evolve perpendicular to the flow direction (since the fluid streams encounter less resistance during the formation of fluid channels within the grain pack). The third case (random orientation) lies in between the two former cases (parallel and orthogonal). All three curves begin and end at the same point, indicating that the initial (when none of the K-feldspar grains are dissolved) and final (when all of the K-feldspar grains are dissolved) permeability values in the same multigrain pack will remain constant regardless of the orientation of the dissolving grains.

We remark that a comprehension of the effect of etch-pits along random crystallographic planes of K-feldspar grains on the porosity and permeability relationship is not straightforward, as the scale of our digital sandstone is not necessarily representative (due to the limitation of computational workforce) and the results of this analysis



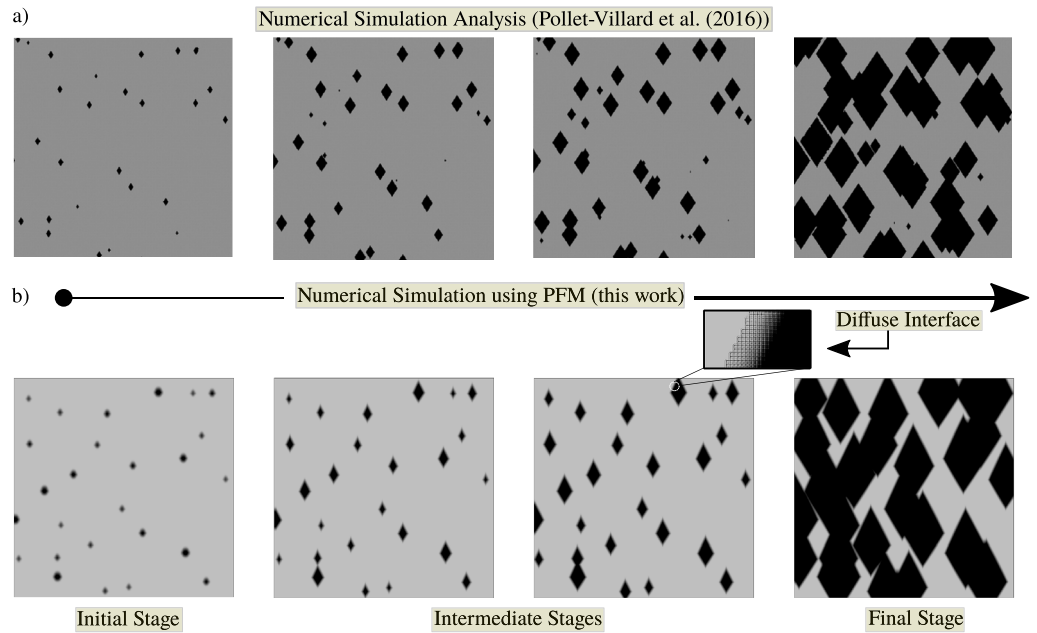


**Figure 4.** Etch-pit growth in numerical 2D section (representing (0 0 1) plane of K-feldspar). Comparison of (a) the numerical studies from the work of Pollet-Villard, Daval, Fritz, et al. (2016) and (b) the results of our simulation approach using PFM. (a) *Reprinted from* Pollet-Villard, Daval, Fritz, et al. (2016), *Copyright 2016, with permission from Elsevier.*

may not be applicable to large-scale grain packs (where more complicated behaviors can be seen). In an ideal situation, all outcome data sets of randomly developed pits would lay somewhere between the above two cases (parallel and orthogonal), however this is not the case in all instances, and thus one output data-point (random case) lies outside the desired limit (as indicated by simulation studies (Figure 10b)). The work of Prajapati, Abad Gonzalez et al. (2020) discusses porosity-permeability curves, and shows comparable (but opposite) characteristics. As quartz grains are syntaxially overgrown, decreasing porosity, our results follow a similar but opposite trend as grains are dissolved. While it is well documented, that the dissolution of detrital grains (including K-feldspar)

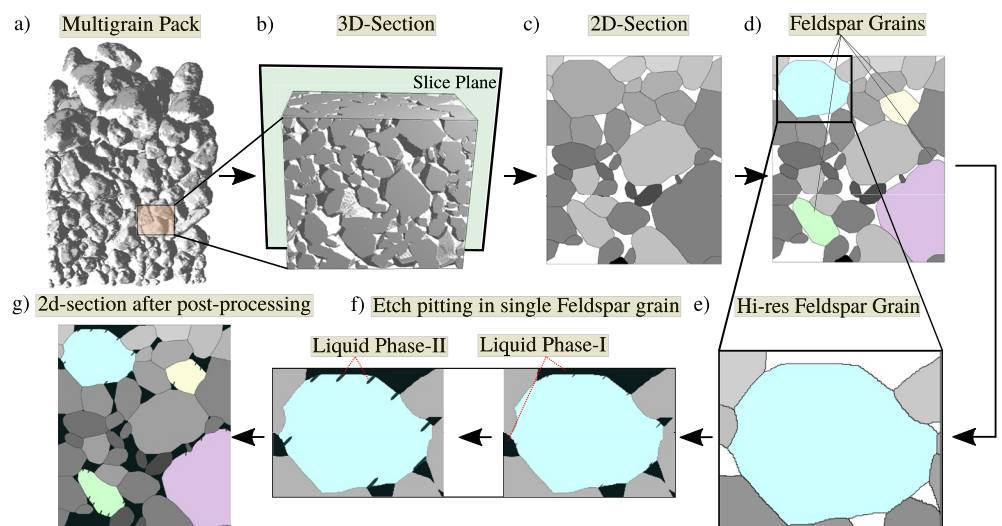


**Figure 5.** Novel workflow used in this simulative analysis. (a) A numerical porous sandstone (adapted from the work of Prajapati, Abad Gonzalez et al. (2020)). (b) 3D-section (extracted from sandstone in a). (c) 2D-section (sliced and extracted from 3D-section in b)). (d) K-feldspar grains embedded in 2D-section (in highlighted colors). (e) High-resolution K-feldspar grain (increasing grid resolution of every K-feldspar grain individually). (f) Etch-pits" evolution in hi-res K-feldspar grain. (g) Embedding different stages of K-feldspar grains' dissolution into 2D-section (using post-processing tools).

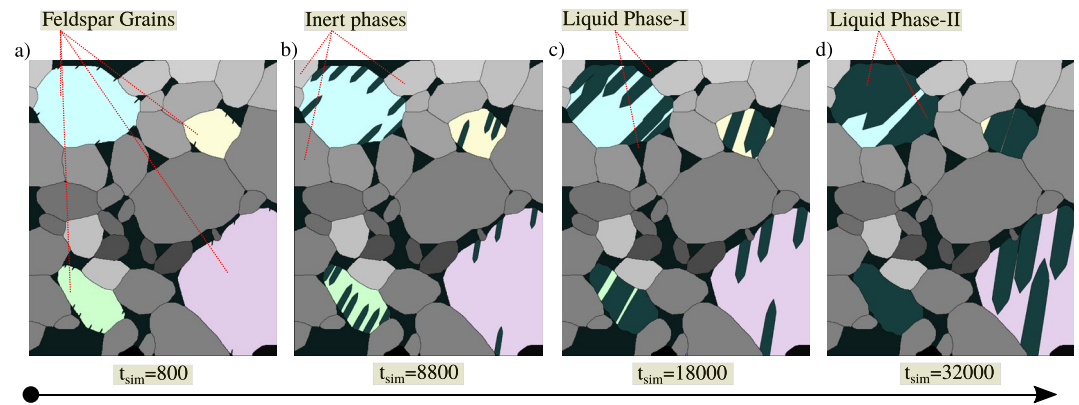


**Figure 6.** Etch-pit evolution in a 2D-domain at different simulation time-steps.

generally enhances the available pore space (e.g., Ma et al., 2017; Mansurbeg et al., 2008), the correlation to permeability is not as straight forward. Ma et al. (2017) report that porosity is generally enhanced, where more dissolution porosity in K-feldspar grain is formed. However, at the same porosities, samples containing less intragranular dissolution porosity in feldspars (0%–1% compared to 2%–3%) have higher permeabilities (Ma et al., 2017). This can be related to the precipitation of alteration products from feldspar dissolution, most likely to the precipitation of fibrous illite (Ma et al., 2017). Although illite is present in the studied natural reference samples from the Buntsandstein, its formation is not necessarily related to feldspar dissolution, but has been related to hydrothermal fluid flow phases (Clauer et al., 2008) and often predates feldspar dissolution in the studied samples (Busch, Adelman, et al., 2022; Busch, Spitzner, et al., 2022) (also see, Figure 1).

However, when comparing the porosity and permeability data for natural samples with a variable porosity and permeability distribution, an exponential correlation can be observed (Figure 11). Increased porosity generally correlates with increased permeability. Based on the different exponents derived in natural data-sets, some sample series from the Permian Penrith Sandstone (United Kingdom, Monsees et al. (2021)) and the Triassic

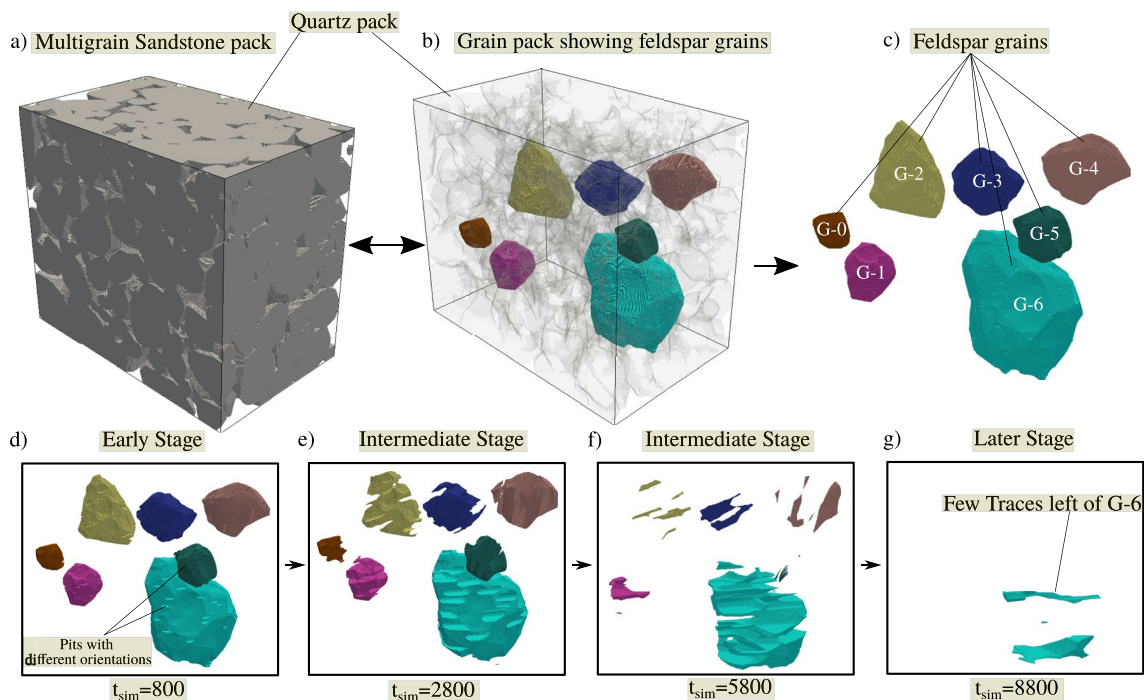


**Figure 7.** Dissolution of K-feldspar grains embedded in sandstone, using the same workflow as presented in detail Figures 5a–5c shows extraction of K-feldspar grains. (d–g) Temporal evolution of K-feldspar dissolution.

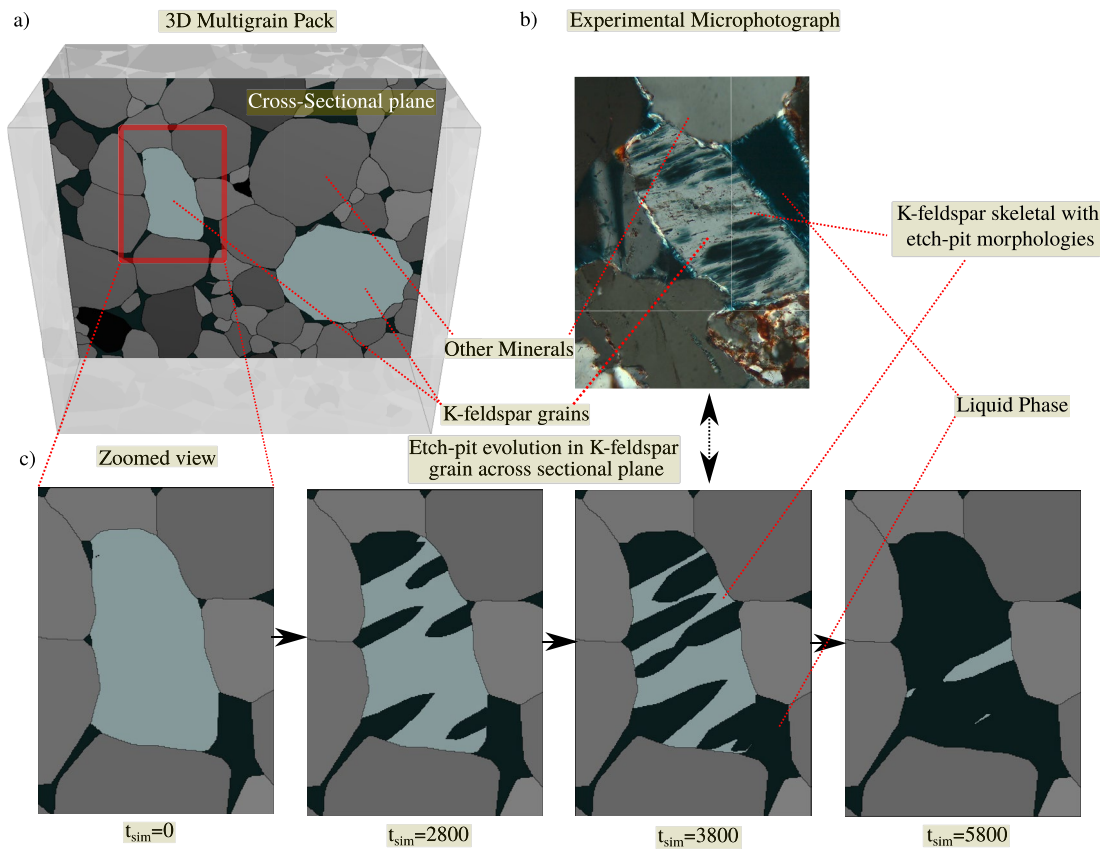


**Figure 8.** Comparison of numerical simulation results to natural rock structure. (a) Initial numerical sandstone, (b) thin section of partially dissolved feldspar grain in Buntsandstein sandstone showing the diamond-shaped etch-pits in 2D, and (c) temporal evolution of etch-pit dissolution.

Buntsandstein (Germany, Busch, Adelman et al. (2022); Busch, Spitzner, et al. (2022)) show a larger increase in permeability per unit of additional porosity in the sandstones. Over the range of gained porosity of the simulation results (+7.25%) permeability increases by nearly two orders of magnitude, while permeability in the samples just affected by feldspar dissolution is increased by less than one order of magnitude. On the other hand a sample series from the Permian Rotliegend (Busch et al., 2020) shows a more comparable increase in permeability per unit of additional porosity (one order of magnitude). These digital twin simulations, thus can deliver the specific influence of intragranular dissolution by etch-pit formation on permeability, which is much less than if the bulk porosity is increased, as only individual grains are dissolved, only affecting individual pore throat diameters, which are the main control on fluid pathway restrictions, as also derived from previous studies (Pittman, 1979). Nevertheless, these simulations can derive the impact of feldspar dissolution in three dimensional grain packs on permeability.

## 5. Concluding Remarks

The present work serves as one of the first three-dimensional numerical investigation, addressing the etch-pitting dissolution phenomenon in K-feldspar grains, which are present in different proportions in sandstones, using a thermodynamically consistent multiphase-field model. In this work, we identified the facet-specific anisotropy model parameters based on experimental works of Pollet-Villard, Daval, Fritz, et al. (2016), and determined the kinetic anisotropy model parameters by simulating the growth of an etch-pit in a K-feldspar grain. The calibrated model is able to:

- Simulate the formation and growth of diamond-shaped pit morphology, consistent with the above mentioned work.
- Recover the relative growth rates of different facets as found in the experiments of Pollet-Villard, Daval, Fritz, et al. (2016).

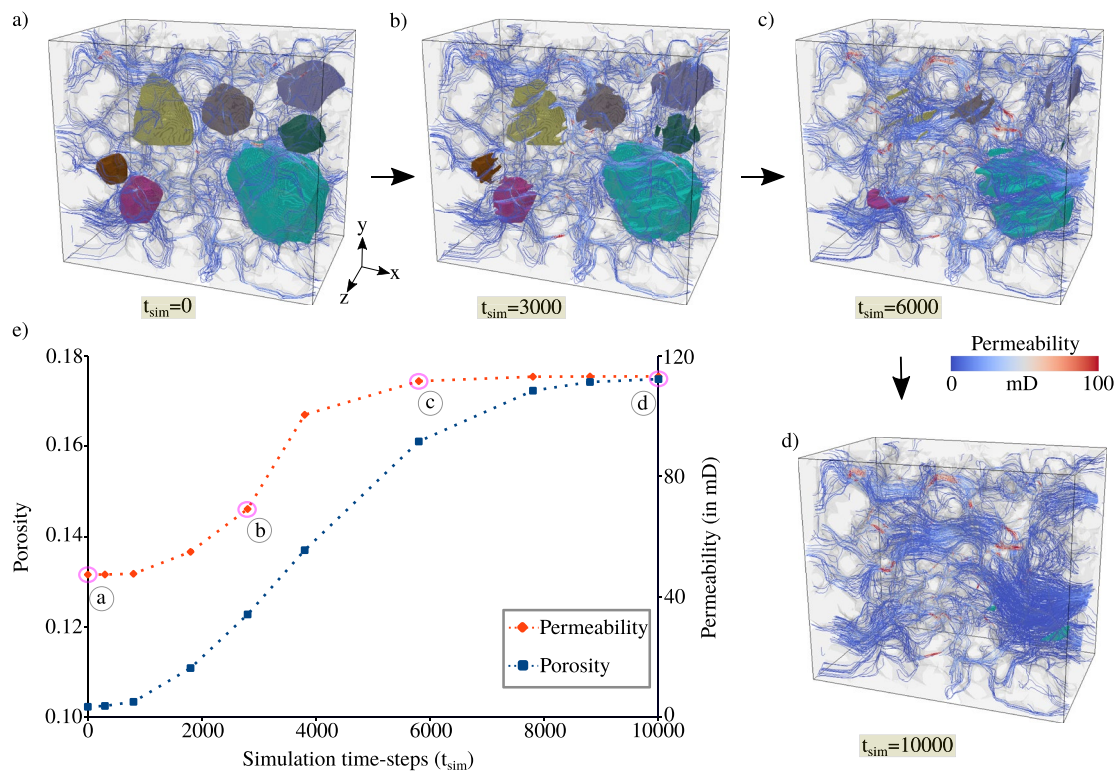


**Figure 9.** a-d) Representing fluid evolution as the K-feldspar grains dissolves (visualized with stream-lines), and e) corresponding porosity (left y-axis) and permeability (right y-axis) evolution plot versus simulation time-steps (x-axis).

Next, we performed simulation of the growth of multiple etch-pits in a 2D section. The simulated etch-pitting resembles the above mentioned numerical experiments, in terms of facet formation and merging of etch-pits. Furthermore, we devised an up-scaling workflow in order to overcome the following two computational challenges:

- Resolution of the microscopic etch-pits within the 1,000 times larger grain pack, and
- Nucleation of etch-pits along the cleavage planes of K-feldspar grains, utilizing a single fluid phase present in and around the sandstone pack.

The presented workflow enables the simulation of etch-pitting in multigrain packs in 3D, analogous to sandstones containing quartz and K-feldspar grains. The simulated pit-growth in the multigrain pack shows clear

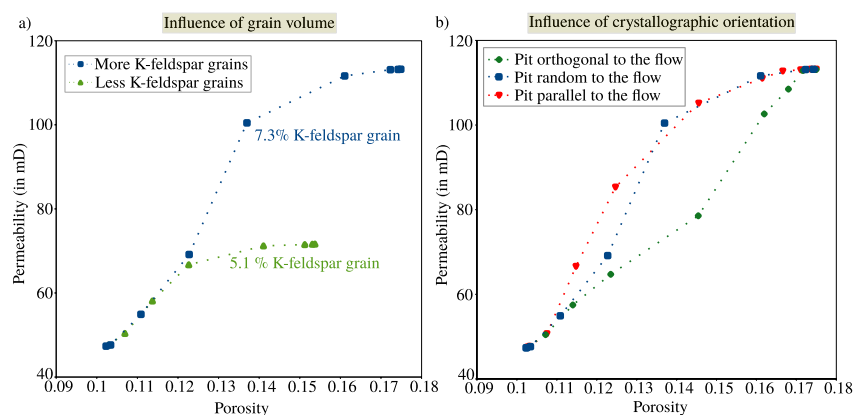


**Figure 10.** Porosity-Permeability correlation of (a) the impact of the volume of dissolving K-feldspar grains present in the system (5.1 and 7.3%) and (b) the influence of the crystallographic orientations of the grains (for pit evolution) for a K-feldspar content of 7.3%.



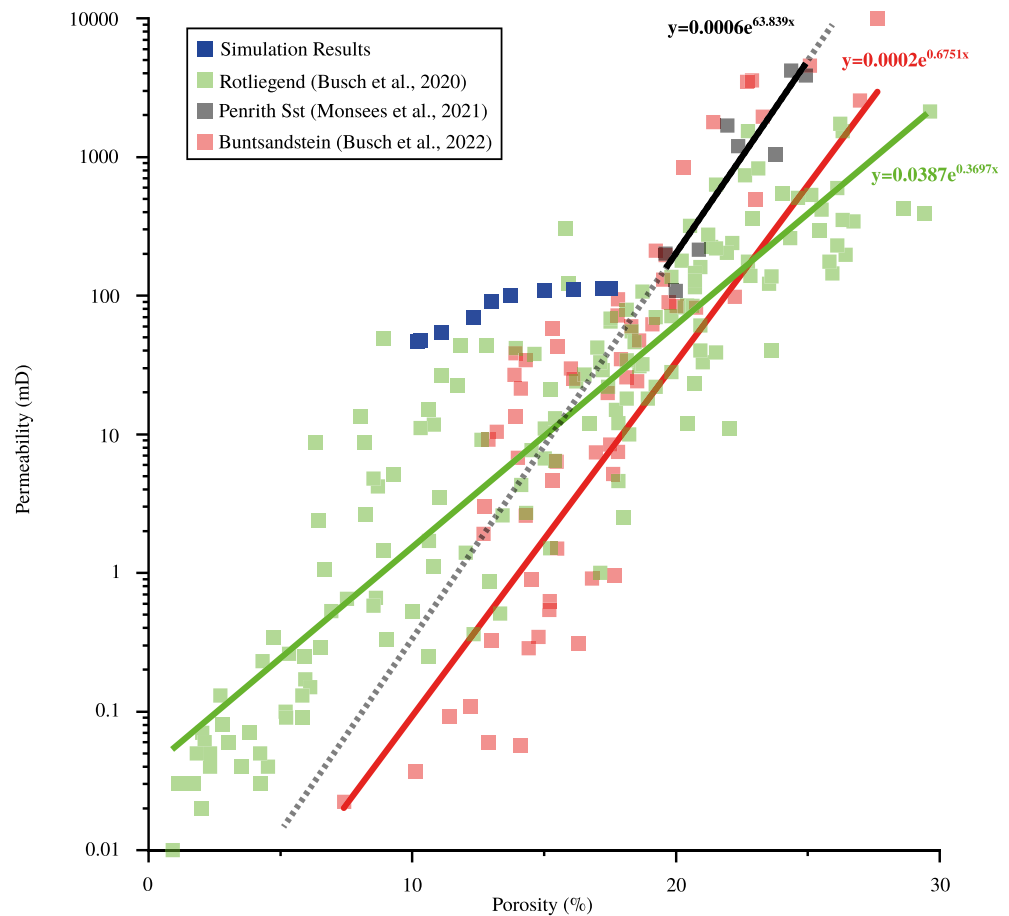


**Figure 11.** A logarithmic plot displaying the porosity-permeability correlation, as well as a comparison of the derived simulation results from this study with other experimental findings.

similarities with the thin section microphotographs in terms of formation of skeletal K-feldspar remnants. Finally, 3D numerical experiments of etch-pitting were performed in grain packs comprising of different fractions and crystallographic orientations of K-feldspar grains. The detailed analysis of the generated data-sets revealed the following:

- Increasing K-feldspar content in sandstones can significantly affect the permeability for the given porosity at certain time, and
- As the orientation of K-feldspar grains aligns parallel to the fluid-flow direction, this plays an important role in the evolution of fluid-path inside the sandstone, hence improving permeability for a given porosity.

Depending on the degree of dissolution of K-feldspar grains (0 – 100%), these simulations enable to specifically attribute the degree of permeability increase to dissolution processes, as the comparative thin sections still contain skeletal remnants and are not completely dissolved. Although the current model considers only qualitative simulation-based analysis regarding the etch-pitting phenomenon of K-feldspar grains and related analysis, we note that with more experimentally based data, the modeling can also be done quantitatively (inclusion of physical time-scale), adding more insight for future scientific work. Moreover, by incorporating the solute concentration into the presented framework, the effect of varying the average flow velocity on the dissolution of the K-feldspar grain would be possible. This might also enable us to predict the computation of numerous dimensionless numbers. In addition, integrating the effect of fluid salinity into the dissolution model can be an interesting model extension, as this will result in a much more accurate calibration of the driving force of dissolution (which is treated as constant in this work), as the actual fluid characteristic can be taken into account to provide more precise insights. The current study sets the path for more sophisticated dissolution modeling for other minerals as well, for applications such as reservoir quality modeling and prediction. One interesting idea

for the future of this work is to combine it with the work of Prajapati et al. (2021) to show how different minerals dissolve in the same domain at different rates.

## Appendix A

Table A1 shows the list of vectors chosen for the capillary shape of etch-pits. In Table A2 the list of vectors chosen for the kinetic shape of etch-pits are given.

**Table A1**  
The 12 Polyhedral Vertex Vectors of the Capillary Shape

Upper part ( $z > 0$ )			Center part ( $z = 0$ )			Lower Part ( $z < 0$ )		
x	y	z	x	y	z	x	y	z
0	-0.33	0.33	0	0.79	0	0	-0.33	-0.33
0.1566	0	0.33	-0.51	0	0	0.1566	0	-0.33
0	0.2633	0.33	0	-1	0	0	0.2633	-0.33
-0.17	0	0.33	0.47	0	0	-0.17	0	-0.33

**Table A2**  
The 12 Polyhedral Vertex Vectors of the Kinetic Shape

Upper part ( $z > 0$ )			Center part ( $z = 0$ )			Lower Part ( $z < 0$ )		
x	y	z	x	y	z	x	y	z
0	0.60	0.08	0	0.79	0	0	0.60	-0.08
-0.36	0	0.08	-0.51	0	0	-0.36	0	-0.08
0	-0.71	0.08	0	-1	0	0	-0.71	-0.08
0.32	0	0.08	0.47	0	0	0.32	0	-0.08

## Data Availability Statement

For the production of simulation data sets, the PACE3D software package was used. The software license may be acquired at Steinbeis Network ([www.steinbeis.de](http://www.steinbeis.de)) under the administration of Britta Nestler and Michael Selzer in the “Material Simulation and Process Optimization” particular subject. The whole data set is available in the open-access repository located at Kumar et al. (2022).

## Acknowledgments

We thank Helmholtz association for funding the main parts of the modeling and simulation research work under the program “MTET: 38.04.04.” We thankfully acknowledge the constructive review comments by two anonymous reviewers and editorial handling by Douglas Schmitt. The authors acknowledge support by the state of Baden-Württemberg through bwHPC. Open Access funding enabled and organized by Projekt DEAL.

## References

- Anbeek, C., Van Breemen, N., Meijer, E. L., & Van Der Plas, L. (1994). The dissolution of naturally weathered feldspar and quartz. *Geochimica et Cosmochimica Acta*, 58(21), 4601–4613. [https://doi.org/10.1016/0016-7037\(94\)90194-5](https://doi.org/10.1016/0016-7037(94)90194-5)
- Ankit, K., Nestler, B., Selzer, M., & Reichardt, M. (2013). Phase-field study of grain boundary tracking behavior in crack-seal microstructures. *Contributions to Mineralogy and Petrology*, 166(6), 1709–1723. <https://doi.org/10.1007/s00410-013-0950-x>
- Ankit, K., Selzer, M., Hilgers, C., & Nestler, B. (2015). Phase-field modeling of fracture cementation processes in 3-D. *Journal of Geophysical Research: Solid Earth*, 4(2), 79–96. <https://doi.org/10.12783/jpsr.2015.0402.04>
- Ankit, K., Urai, J. L., & Nestler, B. (2015). Microstructural evolution in bitaxial crack-seal veins: A phase-field study. *Journal of Geophysical Research: Solid Earth*, 120(5), 3096–3118. <https://doi.org/10.1002/2015jb011934>
- Arvidson, R. S., Ertan, I. E., Amonette, J. E., & Lüttge, A. (2003). Variation in calcite dissolution rates: A fundamental problem? *Geochimica et Cosmochimica Acta*, 67(9), 1623–1634. [https://doi.org/10.1016/s0016-7037\(02\)01177-8](https://doi.org/10.1016/s0016-7037(02)01177-8)
- Baruch, E. T., Kennedy, M. J., Löhr, S. C., & Dewhurst, D. N. (2015). Feldspar dissolution-enhanced porosity in paleoproterozoic shale reservoir facies from the Barney creek formation (McArthur basin, Australia). *AAPG Bulletin*, 99(9), 1745–1770. <https://doi.org/10.1306/04061514181>
- Becker, I., Busch, B., Koehrer, B., Adelmann, D., & Hilgers, C. (2019). Reservoir quality evolution of upper carboniferous (Westphalian) tight gas sandstones, lower saxony basin, NW Germany. *Journal of Petroleum Geology*, 42(4), 371–392. <https://doi.org/10.1111/jpg.12742>
- Beig, M. S., & Lüttge, A. (2006). Albite dissolution kinetics as a function of distance from equilibrium: Implications for natural feldspar weathering. *Geochimica et Cosmochimica Acta*, 70(6), 1402–1420. <https://doi.org/10.1016/j.gca.2005.10.035>
- Berner, R. A., Sjöberg, E., Velbel, M. A., & Krom, M. D. (1980). Dissolution of pyroxenes and amphiboles during weathering. *Science*, 207(4436), 1205–1206. <https://doi.org/10.1126/science.207.4436.1205>

- Bjørlykke, K., Mo, A., & Palm, E. (1988). Modelling of thermal convection in sedimentary basins and its relevance to diagenetic reactions. *Marine and Petroleum Geology*, 5(4), 338–351. [https://doi.org/10.1016/0264-8172\(88\)90027-x](https://doi.org/10.1016/0264-8172(88)90027-x)
- Bouissonnié, A., Daval, D., Marinoni, M., & Ackerer, P. (2018). Comparison between reactive-transport simulations and calcite dissolution experiments highlights the importance of fluid flow in upscaling studies. In *Egu General Assembly Conference Abstracts* (p. 6206).
- Bringedal, C., von Wolff, L., & Pop, I. S. (2020). Phase field modeling of precipitation and dissolution processes in porous media: Upscaling and numerical experiments. *Multiscale Modeling and Simulation*, 18(2), 1076–1112. <https://doi.org/10.1137/19m1239003>
- Busch, B., Adelmann, D., Herrmann, R., & Hilgers, C. (2022). Controls on compactional behavior and reservoir quality in a triassic Buntsandstein reservoir, upper rhine graben, SW Germany. *Marine and Petroleum Geology*, 136, 105437. <https://doi.org/10.1016/j.marpetgeo.2021.105437>
- Busch, B., Hilgers, C., & Adelmann, D. (2020). Reservoir quality controls on Rotliegend fluvio-aeolian wells in Germany and The Netherlands, Southern Permian Basin – Impact of grain coatings and cements. *Marine and Petroleum Geology*, 112, 104075. <https://doi.org/10.1016/j.marpetgeo.2019.104075>
- Busch, B., Spitzner, A.-D., Adelmann, D., & Hilgers, C. (2022). The significance of outcrop analog data for reservoir quality assessment: A comparative case study of lower triassic Buntsandstein sandstones in the upper rhine graben. *Marine and Petroleum Geology*, 141, 105701. <https://doi.org/10.1016/j.marpetgeo.2022.105701>
- Chen, L.-Q. (2002). Phase-field models for microstructure evolution. *Annual Review of Materials Research*, 32(1), 113–140. <https://doi.org/10.1146/annurev.matsci.32.112001.132041>
- Chen, X., Thornton, S. F., & Small, J. (2015). Influence of hyper-alkaline pH leachate on mineral and porosity evolution in the chemically disturbed zone developed in the near-field host rock for a nuclear waste repository. *Transport in Porous Media*, 107(2), 489–505. <https://doi.org/10.1007/s11242-014-0450-0>
- Choudhury, A. (2017). Phase-field modeling as a method relevant for modeling phase transformation during interdiffusion. In *Handbook of solid state diffusion* (Vol. 1, pp. 363–389). Elsevier
- Clauer, N., Liewig, N., Ledesert, B., & Zwingmann, H. (2008). Thermal history of Triassic sandstones from the Vosges Mountains-Rhine Graben rift area, NE France, based on K-Ar illite dating. *Clay Minerals*, 43(3), 363–379. <https://doi.org/10.1180/claymin.2008.043.3.03>
- Dong, Y., Cao, S., Cheng, X., Liu, J., & Cao, H. (2019). Grain-size reduction of feldspar and flow of deformed granites within the Gaoligong shear zone, southwestern Yunnan, China. *Science China Earth Sciences*, 62(9), 1379–1398. <https://doi.org/10.1007/s11430-018-9351-8>
- Doyen, P. M. (1988). Permeability, conductivity, and pore geometry of sandstone. *Journal of Geophysical Research*, 93(B7), 7729–7740. <https://doi.org/10.1029/jb093ib07p07729>
- Emmanuel, S., & Berkowitz, B. (2007). Effects of pore-size controlled solubility on reactive transport in heterogeneous rock. *Geophysical Research Letters*, 34(6), L06404. <https://doi.org/10.1029/2006gl028962>
- Fischer, C., Arvidson, R. S., & Lüttge, A. (2012). How predictable are dissolution rates of crystalline material? *Geochimica et Cosmochimica Acta*, 98, 177–185. <https://doi.org/10.1016/j.gca.2012.09.011>
- Fischer, C., & Lüttge, A. (2018). Pulsating dissolution of crystalline matter. *Proceedings of the National Academy of Sciences*, 115(5), 897–902. <https://doi.org/10.1073/pnas.1711254115>
- Fix, G. J. (1982). Phase field methods for free boundary problems.
- Gautier, J.-M., Oelkers, E. H., & Schott, J. (1994). Experimental study of K-feldspar dissolution rates as a function of chemical affinity at 150°C and pH 9. *Geochimica et Cosmochimica Acta*, 58(21), 4549–4560. [https://doi.org/10.1016/0016-7037\(94\)90190-2](https://doi.org/10.1016/0016-7037(94)90190-2)
- Gout, R., Oelkers, E. H., Schott, J., & Wick, A. (1997). The surface chemistry and structure of acid-leached albite: New insights on the dissolution mechanism of the alkali feldspars. *Geochimica et Cosmochimica Acta*, 61(14), 3013–3018. [https://doi.org/10.1016/s0016-7037\(97\)00122-1](https://doi.org/10.1016/s0016-7037(97)00122-1)
- Hellmann, R., & Tisserand, D. (2005). Feldspar dissolution rates and the Gibbs free energy of reaction. *Geochimica et Cosmochimica Acta - Supplement*, 69(10), A780.
- Hötzer, J., Reiter, A., Hierl, H., Steinmetz, P., Selzer, M., & Nestler, B. (2018). The parallel multi-physics phase-field framework PACE3D. *Journal of Computational Science*, 26, 1–12. <https://doi.org/10.1016/j.jocs.2018.02.011>
- Huang, S.-J., Wu, W.-H., Liu, J., Shen, L.-C., & Huang, C.-G. (2003). Generation of secondary porosity by meteoric water during time of subaerial exposure: An example from yanchang formation sandstone of triassic of Ordos basin. *Earth Science/Diqiu Kexue*, 28(4), 419–424.
- Kang, X., Hu, W., Cao, J., Jin, J., Wu, H., Zhao, Y., & Wang, J. (2018). Selective dissolution of alkali feldspars and its effect on Lower Triassic sandy conglomerate reservoirs in the Junggar Basin, northwestern China. *Geological Journal*, 53(2), 475–499. <https://doi.org/10.1002/gj.2905>
- Keith, R., & Gilman, J. (1960). Dislocation etch pits and plastic deformation in calcite. *Acta Metallurgica*, 8(1), 1–10. [https://doi.org/10.1016/0001-6160\(60\)90132-2](https://doi.org/10.1016/0001-6160(60)90132-2)
- Kumar, A., Prajapati, N., Späth, M., Busch, B., Schneider, D., Hilgers, C., & Nestler, B. (2022). Data set for phase-field studies of K-feldspar dissolution through etch-pit formation. *Zenodo*. <https://doi.org/10.5281/zenodo.7143113>
- Kurganskaya, I., Arvidson, R. S., Fischer, C., & Lüttge, A. (2012). Does the stepwave model predict mica dissolution kinetics? *Geochimica et Cosmochimica Acta*, 97, 120–130. <https://doi.org/10.1016/j.gca.2012.08.033>
- Kurganskaya, I., Rohlf, R., & Lüttge, A. (2023). Multi-scale modeling of crystal-fluid interactions: State-of-the-art, challenges and prospects.
- Lange, I., Toro, M., Arvidson, R. S., Kurganskaya, I., & Lüttge, A. (2021). The role of crystal heterogeneity in alkali feldspar dissolution kinetics. *Geochimica et Cosmochimica Acta*, 309, 329–351. <https://doi.org/10.1016/j.gca.2021.06.032>
- Langer, J. (1980). Instabilities and pattern formation in crystal growth. *Reviews of Modern Physics*, 52(1), 1–28. <https://doi.org/10.1103/revmodphys.52.1>
- Langer, J. (1986). Models of pattern formation in first-order phase transitions. In *Directions in condensed matter physics: Memorial volume in honor of shang-keng ma* (pp. 165–186). World Scientific.
- Lanson, B., Beaufort, D., Berger, G., Bauer, A., Cassagnabere, A., & Meunier, A. (2002). Authigenic kaolin and illitic minerals during burial diagenesis of sandstones: A review. *Clay Minerals*, 37(1), 1–22. <https://doi.org/10.1180/0009855023710014>
- Lasaga, A. C., & Lüttge, A. (2001). Variation of crystal dissolution rate based on a dissolution stepwave model. *Science*, 291(5512), 2400–2404. <https://doi.org/10.1126/science.1058173>
- Lasaga, A. C., & Lüttge, A. (2004). Mineralogical approaches to fundamental crystal dissolution kinetics. *American Mineralogist*, 89(4), 527–540. <https://doi.org/10.2138/am-2004-0407>
- Lei, X., Yongmin, S., Changsheng, X., Yue, Y., Hong, L., & Zhi, C. (2013). Influences of feldspars on the storage and permeability conditions in tight oil reservoirs: A case study of chang-6 group, Ordos basin. *Petroleum Exploration and Development*, 40(4), 481–487. [https://doi.org/10.1016/s1876-3804\(13\)60061-0](https://doi.org/10.1016/s1876-3804(13)60061-0)
- Li, S., Yao, J., Mou, W., Luo, A., Wang, Q., Deng, X., et al. (2018). The dissolution characteristics of the Chang 8 tight reservoir and its quantitative influence on porosity in the Jiuyan area, Ordos Basin, China. *Journal of Natural Gas Geoscience*, 3(2), 95–108. <https://doi.org/10.1016/j.jnggs.2018.04.002>

- Liu, S., Chen, A., Shen, Z., Lv, Z., & Zhang, X. (2018). Fluid-rock interaction and dissolution of feldspar in the upper triassic Xujiahe tight sandstone, Western sichuan basin, China. *Open Geosciences*, *10*(1), 234–249. <https://doi.org/10.1515/geo-2018-0018>
- Long, D. (2017). Provenance of chert rudites and arenites in the northern Canadian cordillera. In *Sediment provenance* (pp. 297–324). Elsevier.
- Ma, B., Cao, Y., & Jia, Y. (2017). Feldspar dissolution with implications for reservoir quality in tight gas sandstones: Evidence from the eocene Es4 interval, dongying depression, bohai bay basin, China. *Journal of Petroleum Science and Engineering*, *150*, 74–84. <https://doi.org/10.1016/j.petrol.2016.11.026>
- MacInnis, I. N., & Brantley, S. L. (1992). The role of dislocations and surface morphology in calcite dissolution. *Geochimica et Cosmochimica Acta*, *56*(3), 1113–1126. [https://doi.org/10.1016/0016-7037\(92\)90049-o](https://doi.org/10.1016/0016-7037(92)90049-o)
- MacInnis, I. N., & Brantley, S. L. (1993). Development of etch pit size distributions on dissolving minerals. *Chemical Geology*, *105*(1–3), 31–49. [https://doi.org/10.1016/0009-2541\(93\)90117-2](https://doi.org/10.1016/0009-2541(93)90117-2)
- Mansurbeg, H., Morad, S., Salem, A., Marfil, R., El-Ghali, M., Nystuen, J., et al. (2008). Diagenesis and reservoir quality evolution of palaeocene deep-water, marine sandstones, the Shetland-Faroes Basin, British continental shelf. *Marine and Petroleum Geology*, *25*(6), 514–543. <https://doi.org/10.1016/j.marpetgeo.2007.07.012>
- Monsees, A. C., Busch, B., & Hilgers, C. (2021). Compaction control on diagenesis and reservoir quality development in red bed sandstones: A case study of permian Rotliegend sandstones. *International Journal of Earth Sciences*, *110*(5), 1683–1711. <https://doi.org/10.1007/s00531-021-02036-6>
- Monsees, A. C., Subhedar, A., Busch, B., Nestler, B., & Hilgers, C. (2020). Calibrating micro-computed tomography data to permeability experiments and petrography - Insights from Digital Rocks. *Oil Gas*, *28*.
- Nestler, B., Garcke, H., & Stinner, B. (2005). Multicomponent alloy solidification: Phase-field modeling and simulations. *Physical Review E*, *71*(4), 041609. <https://doi.org/10.1103/physreve.71.041609>
- Osher, S., & Sethian, J. A. (1988). Fronts propagating with curvature-dependent speed: Algorithms based on Hamilton-Jacobi formulations. *Journal of Computational Physics*, *79*(1), 12–49. [https://doi.org/10.1016/0021-9991\(88\)90002-2](https://doi.org/10.1016/0021-9991(88)90002-2)
- Pers, J., Barwiński, B., Grodzicki, M., & Ciszewski, A. (2016). Afm studies of pits formation on kbr (1 0 0) during its dissolution by water. *Materials Science-Poland*, *34*(4), 863–867. <https://doi.org/10.1515/msp-2016-0108>
- Pittman, E. D. (1979). Porosity, diagenesis and productive capability of sandstone reservoirs. In *Aspects of diagenesis*. SEPM Society for Sedimentary Geology.
- Pollet-Villard, M., Daval, D., Ackerer, P., Saldi, G. D., Wild, B., Knauss, K. G., & Fritz, B. (2016). Does crystallographic anisotropy prevent the conventional treatment of aqueous mineral reactivity? A case study based on K-feldspar dissolution kinetics. *Geochimica et Cosmochimica Acta*, *190*, 294–308. <https://doi.org/10.1016/j.gca.2016.07.007>
- Pollet-Villard, M., Daval, D., Fritz, B., Knauss, K. G., Schäfer, G., & Ackerer, P. (2016). Influence of etch pit development on the surface area and dissolution kinetics of the orthoclase (001) surface. *Chemical Geology*, *447*, 79–92. <https://doi.org/10.1016/j.chemgeo.2016.09.038>
- Prajapati, N., Abad Gonzalez, A., Selzer, M., Nestler, B., Busch, B., & Hilgers, C. (2020). Quartz cementation in polycrystalline sandstone: Insights from phase-field simulations. *Journal of Geophysical Research: Solid Earth*, *125*(2), e2019JB019137. <https://doi.org/10.1029/2019jb019137>
- Prajapati, N., Herrmann, C., Späth, M., Schneider, D., Selzer, M., & Nestler, B. (2020). Brittle anisotropic fracture propagation in quartz sandstone: Insights from phase-field simulations. *Computational Geosciences*, *24*(3), 1361–1376. <https://doi.org/10.1007/s10596-020-09956-3>
- Prajapati, N., Selzer, M., & Nestler, B. (2017). Computational modeling of calcite cementation in saline limestone aquifers: A phase-field study. *Geothermal Energy*, *5*(1), 1–18. <https://doi.org/10.1186/s40517-017-0072-1>
- Prajapati, N., Selzer, M., Nestler, B., Busch, B., & Hilgers, C. (2018). Modeling fracture cementation processes in calcite limestone: A phase-field study. *Geothermal Energy*, *6*(1), 1–15. <https://doi.org/10.1186/s40517-018-0093-4>
- Prajapati, N., Selzer, M., Nestler, B., Busch, B., Hilgers, C., & Ankit, K. (2018). Three-dimensional phase-field investigation of pore space cementation and permeability in quartz sandstone. *Journal of Geophysical Research: Solid Earth*, *123*(8), 6378–6396. <https://doi.org/10.1029/2018jb015618>
- Prajapati, N., Späth, M., Knecht, L., Selzer, M., & Nestler, B. (2021). Quantitative phase-field modeling of faceted crystal dissolution processes. *Crystal Growth & Design*, *21*(6), 3266–3279. <https://doi.org/10.1021/acs.cgd.0c01715>
- Ray, N., Oberlander, J., & Frolkovic, P. (2019). Numerical investigation of a fully coupled micro-macro model for mineral dissolution and precipitation. *Computational Geosciences*, *23*(5), 1173–1192. <https://doi.org/10.1007/s10596-019-09876-x>
- Rijniers, L., Huinink, H., Pel, L., & Kopinga, K. (2005). Experimental evidence of crystallization pressure inside porous media. *Physical Review Letters*, *94*(7), 075503. <https://doi.org/10.1103/physrevlett.94.075503>
- Schindler, M., Hawthorne, F. C., Mandaliev, P., Burns, P. C., & Maurice, P. (2011). An integrated study of uranyl mineral dissolution processes: Etch pit formation, effects of cations in solution, and secondary precipitation. *Radiochimica Acta*, *99*(2), 79–94. <https://doi.org/10.1524/ract.2011.1802>
- Snyder, R. C., & Doherty, M. F. (2007). Faceted crystal shape evolution during dissolution or growth. *AIChE Journal*, *53*(5), 1337–1348. <https://doi.org/10.1002/aic.11132>
- Sokolova, T. (2013). The destruction of quartz, amorphous silica minerals, and feldspars in model experiments and in soils: Possible mechanisms, rates, and diagnostics (the analysis of literature). *Eurasian Soil Science*, *46*(1), 91–105. <https://doi.org/10.1134/s1064229313010080>
- Späth, M., Spruženiec, L., Urai, J. L., Selzer, M., Arndt, M., & Nestler, B. (2021). Kinematics of crystal growth in single-seal syntaxial veins in limestone - a phase-field study. *Journal of Geophysical Research: Solid Earth*, *126*(10), e2021JB022106. <https://doi.org/10.1029/2021jb022106>
- Späth, M., Urai, J. L., & Nestler, B. (2022a). Formation of radiator structures in quartz veins-Phase-field modeling of multi-crack sealing. *Journal of Structural Geology*, *158*, 104576. <https://doi.org/10.1016/j.jsg.2022.104576>
- Späth, M., Urai, J. L., & Nestler, B. (2022b). Incomplete crack sealing causes localization of fracturing in hydrothermal quartz veins. *Geophysical Research Letters*, *49*(15), e2022GL098643. <https://doi.org/10.1029/2022gl098643>
- Spruženiec, L., Späth, M., Urai, J. L., Ukar, E., Selzer, M., & Nestler, B. (2021). Wide-blocky veins explained by dependency of crystal growth rate on fracture surface type: Insights from phase-field modeling. *Geology*, *49*(6), 641–646. <https://doi.org/10.1130/g48472.1>
- Spruženiec, L., Späth, M., Urai, J. L., Ukar, E., Selzer, M., Nestler, B., & Schwedt, A. (2020). Formation of wide-blocky calcite veins by extreme growth competition. *Journal of the Geological Society*, *178*(2). <https://doi.org/10.1144/jgs2020-104>
- Stoessel, R. K., & Pittman, E. D. (1990). Secondary porosity revisited: The chemistry of feldspar dissolution by carboxylic acids and anions. *AAPG Bulletin*, *74*(12), 1795–1805.
- Sun, Z., Espinoza, D. N., & Balhoff, M. T. (2018). Reservoir rock chemo-mechanical alteration quantified by triaxial tests and implications for fracture reactivation. *International Journal of Rock Mechanics and Mining Sciences*, *106*, 250–258. <https://doi.org/10.1016/j.ijrmm.2018.04.004>
- Surdam, R. C., Boese, S. W., & Crossey, L. J. (1984). The chemistry of secondary porosity: Part 2. Aspects of porosity modification. In D. A. McDonald & R. C. Surdam (Eds.), *Clastic diagenesis*. American Association of Petroleum Geologists.



- Surdam, R. C., Crossey, L. J., Hagen, E. S., & Heasler, H. P. (1989). Organic-inorganic interactions and sandstone diagenesis. *AAPG Bulletin*, 73(1), 1–23.
- Trindade Pedrosa, E., Kurganskaya, I., Fischer, C., & Lutge, A. (2019). A statistical approach for analysis of dissolution rates including surface morphology. *Minerals*, 9(8), 458. <https://doi.org/10.3390/min9080458>
- van Noorden, T. L. (2009). Crystal precipitation and dissolution in a porous medium: Effective equations and numerical experiments. *Multiscale Modeling and Simulation*, 7(3), 1220–1236. <https://doi.org/10.1137/080722096>
- Waldron, K., Lee, M., & Parsons, I. (1994). The microstructures of perthitic alkali feldspars revealed by hydrofluoric acid etching. *Contributions to Mineralogy and Petrology*, 116(3), 360–364. <https://doi.org/10.1007/bf00306504>
- Wendler, F., Okamoto, A., & Blum, P. (2016). Phase-field modeling of epitaxial growth of polycrystalline quartz veins in hydrothermal experiments. *Geofluids*, 16(2), 211–230. <https://doi.org/10.1111/gfl.12144>
- Wilkinson, M., Milliken, K. L., & Haszeldine, R. S. (2001). Systematic destruction of K-feldspar in deeply buried rift and passive margin sandstones. *Journal of the Geological Society*, 158(4), 675–683. <https://doi.org/10.1144/jgs.158.4.675>
- Xiao, M., Yuan, X., Cheng, D., Wu, S., Cao, Z., Tang, Y., & Xie, Z. (2018). Feldspar dissolution and its influence on reservoirs: A case study of the lower triassic baikouquan formation in the northwest margin of the junggar basin. *Geofluids*.
- Xu, Z., Huang, H., Li, X., & Meakin, P. (2012). Phase field and level set methods for modeling solute precipitation and/or dissolution. *Computer Physics Communications*, 183(1), 15–19. <https://doi.org/10.1016/j.cpc.2011.08.005>
- Xu, Z., & Meakin, P. (2008). Phase-field modeling of solute precipitation and dissolution. *The Journal of Chemical Physics*, 129(1), 014705. <https://doi.org/10.1063/1.2948949>
- Yang, S., Ukrainczyk, N., Caggiano, A., & Koenders, E. (2021). Numerical phase-field model validation for dissolution of minerals. *Applied Sciences*, 11(6), 2464. <https://doi.org/10.3390/app11062464>
- Yuan, G., Cao, Y., Gluyas, J., Li, X., Xi, K., Wang, Y., et al. (2015). Feldspar dissolution, authigenic clays, and quartz cements in open and closed sandstone geochemical systems during diagenesis: Typical examples from two sags in bohái bay basin, east China. *AAPG Bulletin*, 99(11), 2121–2154. <https://doi.org/10.1306/07101514004>
- Yuan, G., Cao, Y., Jia, Z., Gluyas, J., Yang, T., Wang, Y., & Xi, K. (2015). Selective dissolution of feldspars in the presence of carbonates: The way to generate secondary pores in buried sandstones by organic CO<sub>2</sub>. *Marine and Petroleum Geology*, 60, 105–119. <https://doi.org/10.1016/j.marpetgeo.2014.11.001>
- Yuan, G., Cao, Y., Schulz, H.-M., Hao, F., Gluyas, J., Liu, K., et al. (2019). A review of feldspar alteration and its geological significance in sedimentary basins: From shallow aquifers to deep hydrocarbon reservoirs. *Earth-Science Reviews*, 191, 114–140. <https://doi.org/10.1016/j.earscirev.2019.02.004>
- Yuan, K., Starchenko, V., Lee, S. S., De Andrade, V., Gursoy, D., Sturchio, N. C., & Fenter, P. (2019). Mapping three-dimensional dissolution rates of calcite microcrystals: Effects of surface curvature and dissolved metal ions. *ACS Earth and Space Chemistry*, 3(5), 833–843. <https://doi.org/10.1021/acsearthspacechem.9b00003>
- Zhang, L., Soong, Y., & Dilmore, R. M. (2016). Investigation on porosity and permeability change of mount simon sandstone (Knox county, IN, USA) under geological CO<sub>2</sub> sequestration conditions: A numerical simulation approach. *Greenhouse Gases: Science and Technology*, 6(4), 574–587. <https://doi.org/10.1002/ghg.1584>
- Zhiyong, G., Jiarui, F., Jinggang, C., Xiaoqi, W., Chuanmin, Z., & Yuxin, S. (2017). Physical simulation and quantitative calculation of increased feldspar dissolution pores in deep reservoirs. *Petroleum Exploration and Development*, 44(3), 387–398. [https://doi.org/10.1016/s1876-3804\(17\)30045-9](https://doi.org/10.1016/s1876-3804(17)30045-9)
- Zhu, C.-S., Ma, F.-l., Lei, P., Han, D., & Feng, L. (2021). Comparison between level set and phase field method for simulating bubble movement behavior under electric field. *Chinese Journal of Physics*, 71, 385–396. <https://doi.org/10.1016/j.cjph.2021.02.012>
- Zhu, X., Wang, Y., Zhong, D., Zhang, Q., Zhang, Z., Zhang, S., & Lv, X. (2007). Pore types and secondary pore evolution of Paleogene reservoir in the Jiyang Sag. *Acta Geologica Sinica*, 81(2), 197–204.